This is a preprint, the final version is subject to change, of the American Mineralogist (MSA)
Cite as Authors (Year) Title. American Mineralogist, in press.
DOI: https://doi.org/10.2138/am-2019-6773

Revision 1

Precipitates of α-cristobalite and silicate glass in UHP clinopyroxene from a Bohemian Massif eclogite

Tina R. Hill[1, 2], Hiromi Konishi[1#], Franklin Hobbs[1], Seungyeol Lee[1], and Huifang Xu[1] *

[1] Department of Geoscience, University of Wisconsin-Madison, Madison, Wisconsin 53706, U.S.A.

[2] Bruker Nano, Inc., 5465 E. Cheryl Parkway, Madison, WI, 53711

[#] Present address: Department of Geology, Niigata University, 8050 Ikarashi 2-no-cho, Nishi-ku, 12 Niigata 950-2181, Japan.

*** Corresponding author: Prof. Huifang Xu**

E-mail: hfxu@geology.wisc.edu

Tel: 608-265-5887

ABSTRACT

Low pressure metastable nano-scale crystals of α-cristobalite have been observed epitaxially-exsolved in cores of UHP clinopyroxene from the Bohemian Massif, Czech Republic. SAED patterns and HRTEM images detail the close structural relationship between host clinopyroxene and α-cristobalite precipitate: $[001]_{Di} \parallel [010]\alpha$, $(010)_{Di} \sim\parallel (101)\alpha$. TEM results indicate that α-cristobalite exsolved from host clinopyroxene. Non-crystalline Al-bearing silicate phases, also exsolved from UHP clinopyroxene, possesses Al/Si ratios close to eutectic compositions in the system $NaAlSi_3O_8$-SiO_2-H_2O system. Presence of glass exsolution suggests a high temperature formation environment and presence of water. The α-cristobalite formed in a localized low-pressure, micro-environment formed through exsolution of vacancies and excess silica from the host pyroxene lattice. This micro-environment may be a result of negative density changes due to excess lower density silica exsolving from higher density pyroxene during an exsolution process that involved no localized volume change. Interface-controlled exsolution via lattice matching at the diopside/cristobalite interface, and stability changes and melting point depression due to nano-scale size effects contributed to formation and persistence of this metastable phase. Amphibole in association with α-cristobalite and some non-crystalline silicate phases may be a clue to localized water quantities; silica exsolution with amphibole may have formed below the eutectic temperature and at a later stage than non-crystalline silicate phases without amphibole. Silica rods in Nové Dvory clinopyroxenes were previously thought to be quartz; however, our investigation reveals a variety of low pressure, high temperature, and/or metastable phases greatly affected by the presence of vacancy and OH in clinopyroxenes. The results will help us better understand OH in the UHP pyroxene and even water release in the mantle.

INTRODUCTION

Discoveries of coesite (Smith 1984) and microdiamond in the Kokchetav Massif (Sobolev and Shatsky 1990) have clearly established that rocks of continental origin were subjected to ultrahigh-pressure metamorphism (UHPM), which required their subduction to a depth of not less than 80-120 km (Chopin 1984; Smith 1984; Schreyer et al. 1987; Sobolev and Shatsky 1990; Xu et al. 1992; Coleman and Wang 1995; Dobrzhinetskaya et al. 1995; Wain 1997; Ye et al. 2000; Van Roermund et al. 2002; Carswell et al. 2006; Dobrzhinetskaya et al. 2006). It is in these deeply-subducted terranes that micro- and nano-scale minerals within stable host minerals such as garnet and pyroxene are often preserved, even though prograde textures and mineral parageneses are typically obliterated during exhumation from great depth. Micro- and nano-scale minerals of these orogenic terranes are of particular interest to investigators because they are windows to the special conditions required to develop UHPM terranes when no other evidence persists, and aids in elucidating the geodynamic processes endured by them.

Crystallographically-oriented silica rods exsolved in clinopyroxene, many coexisting with amphibole, are well-documented from ultrahigh-pressure (UHP) terranes around the world: (Bakun-Czubarow 1992; Bi, et al. 2018; Smith 1984; Gayk et al. 1995; Wain 1997; Katayama et al. 2000; Schmadicke and Muller 2000; Tsai and Liou 2000; Dobrzhinetskaya et al. 2002; Zhu and Ogasawara 2002; Klemd 2003; Song et al. 2003; Janak et al. 2004; Sajeev et al. 2010; Dokukina and Konilov 2011; Konilov et al. 2011; Song et al. 2018). Although there is at present evidence of HP (and not UHP) clinopyroxenes possessing these crystallographically-oriented silica precipitates in the Blue Ridge Mountains, USA, the Kontum Massif, central Vietnam, and the Greek Rhodope (Page et al. 2005; Anderson and Moechner 2007; Nakano et al. 2007a; Nakano et al. 2007b; Proyer et al. 2009; Faryad and Fisera 2015; Li et al. 2018), in the dearth of

other UHP evidence the siliceous rods are often used as indicators of rocks experiencing UHP conditions. The breakdown textures of clinopyroxene and its chemical variations may help us to investigate pre- and post-peak rock evolution of the host rock.

Reports of silica exsolution in clinopyroxene have previously been identified by micro- and macroscale techniques as either coesite or quartz (Bakun-Czubarow 1992). For instance, Zhang et al. (2005) demonstrated that silica exsolution took place in the coesite stability field and that the coesite easily transforms to quartz during retrograde metamorphism. More recently, High-resolution transmission electron microscopy (HRTEM) investigation of crystallographically-oriented silica in clinopyroxenes of the Kokchetav Massif discovered anomalous low pressure silica polymorphs (the first confirmed natural occurrence of keatite) in UHP pyroxene (Hill et al. 2013), but no coesite or quartz.

This study characterized crystallographically-oriented silica in clinopyroxenes from an eclogite of well-established UHP origin from the Bohemian Massif to confirm mineral phase identification of silica exsolution and to understand the processes of this occurrence more thoroughly. As in the Hill et al. (2013) study, this HRTEM investigation has found neither of the expected higher density silica polymorphs coesite or quartz. Instead, low-density and low-pressure phases α-cristobalite and Na-Al silicate glass are observed exsolved from UHP diopside. We explore possible mechanisms of formation for the metastable, low *P*, low *T* α-cristobalite and Al-bearing silica glass.

The terms exsolution, precipitate, and inclusion are used interchangeably by researchers to describe the phenomenon of crystallographically-oriented silica within pyroxene. We opt for "exsolution" in this manuscript to imply that the siliceous rods are likely formed from breakdown of the clinopyroxenes during exhumation. Further information about this is found in

the Discussion section. We have, at times still used the word precipitate as a descriptor when the use of the term "exsolvent" is somewhat cumbersome.

GEOLOGIC BACKGROUND AND SAMPLE DESCRIPTION

Orogenic peridotite bodies are components of metamorphic terranes in most major mountain systems. Some peridotite lenses contain (or contained) garnet-bearing assemblages, particularly where they occur within eclogite-facies metamorphic crustal rocks that recrystallized at high (HP) or ultrahigh (UHP) pressures. They are rich in petrological, mineralogical and geochemical information about the interaction of the mantle with the crust during mountain building (Brueckner and Medaris 1998, 2000; Rampone and Morten 2001; Scambelluri et al. 2008; Spengler et al. 2009). This study focuses on clinopyroxenes of the Nové Dvory eclogite from the Gföhl nappe (340 Ma (van Breemen et al. 1982)), a nappe within the Bohemian Massif in the Czech Republic. Clinopyroxenes in this eclogite exhibit crystallographically-oriented silica in their cores. It is also within the UHP range. Calculated *P-T* estimates of the Gföhl n ppe mantle garnet peridotite (which hosts the thin layers of the Nové Dvory eclogite) have been calculated at 875–1150ºC, 3.3–6 GPa (Medaris et al. 2006). In addition to calculated UHP pressures, microdiamonds have been found as inclusions in garnet, kyanite, and zircon in the Eclogite-Gneiss Unit (Massonne 1998). Coesite has also been found in the Eclogite-Gneiss Unit (Massonne 2001).

The Nové Dvory eclogite is fine- to medium-grained, massive, and generally equigranular. It is composed primarily of Mg-Fe-garnet and Ca-rich clinopyroxene (between omphacite and diopside) (Table 1). A transmitted light micrograph of the rock (eclogite) (Fig. 1a) demonstrates the predominance of garnet and pyroxene. Thin rims of Na-rich clinopyroxene

are observed in electron backscatter images surrounding pyroxenes (arrows, Fig. 1a). Observed accessory minerals are rutile, apatite, zircon, iron sulfides, and iron oxides (possible retrograde phases ilmenite and Mg-bearing ilmenite). Some later-stage retrograde reactions (pyroxene-plagioclase symplectites and amphiboles) are observed at grain boundaries (Fig. 1a), otherwise, the rock is relatively fresh displaying only minor fracturing and alteration.

A plane polarized light image with a clinopyroxene grain oriented at some angle to the *c*-axis (Fig. 1b) displays siliceous phases concentrated in the core. In this orientation silica appears as elongated dark euhedral lines. In contrast, when clinopyroxenes are oriented with the *c*-axis parallel to the viewing direction, they appear as dark euhedral dots. This shape change with differing orientations of pyroxene demonstrates that the precipitates are crystallographically-oriented within the pyroxene lattice. A pyroxene grain boundary at the upper left in Fig. 1b (black circle) demonstrates that silica rods are few near grain boundaries.

EXPERIMENTAL METHODS

High-resolution TEM (HRTEM) images and selected-area electron diffraction patterns (SAED) were obtained utilizing an FEI Titan aberration-corrected S/TEM at the University of Wisconsin-Madison at 200 kV accelerating voltage. In addition to clinopyroxene (CPX) chemical compositions from the electron microprobe, compositions of silica precipitates were also analyzed by means of X-ray energy-dispersive spectroscopy (EDS) with small spot sizes in HRTEM mode using an EDAX EDS system on the FEI Titan S/TEM.

Major element compositions of bulk CPX crystals were determined via wavelength dispersive spectrometry performed with the five spectrometer Cameca SX51 electron microprobe at the University of Wisconsin-Madison. Analytical operating conditions were 15 kV

accelerating voltage, Faraday cup current of 20 nA, and 20 s counting times per element. Beam spot size was 1 μm. Samples and standards were coated with ~20 nm carbon. Microprobe analytical standards were: hematite for Fe, augite for Ca, olivine for Mg, rutile for Ti, chromite for Cr, Mn-olivine for Mn, and hornblende for Si, Na, Al, and K.

Clinopyroxene lattice parameters were refined from X-ray diffraction (XRD) patterns by means of least squares analysis using MDI, Inc. Jade 9.0 software. XRD patterns were collected with a Rigaku Rapid II X-ray diffraction system with a 2-D image plate (Mo Kα radiation), with an accelerating voltage of 50kV, a current of 50 mA, and a 0.1mm diameter collimator. Diffraction data were collected on an image-plate detector. Two-dimensional images were then integrated to produce conventional 2-theta -intensity patterns using Rigaku's 2DP software.

Polished petrographic thin sections (30 μm thick) of the previously described CPX grains were examined to find pyroxenes oriented parallel to the *c*-axis. Clinopyroxene grains were cut out and thinned to ~20 μm by hand with silicon carbide grinding disks. Grains were then mounted on molybdenum TEM grids. These foils were thinned to electron transparency via Ar^+ ion milling in a Fischione 1010 ion mill.

RESULTS

Transmission electron microscope results

A bright-field (BF) TEM image details a nano-crystal of α-cristobalite (Fig. 2). Dominant pyroxene crystallographic planes observed in the $[001]_{Di}$ orientation are labeled {010} and {110}. These planes govern α-cristobalite crystal morphology, which appears in almost all cases as a euhedral 'negative' pyroxene shape. The SAED pattern (Fig. 2b) was calibrated with clinopyroxene lattice parameters calculated from collected X-ray diffraction data from a single crystal of clinopyroxene, then refined via least squares method. Those parameters are: a = 9.630

Å, b = 8.818 Å, c = 5.244 Å, α = γ =90°, β =106.2°. The SAED pattern confirms host diopside, [001], is epitaxially-oriented with α-cristobalite, [010]. Cristobalite *hkl*'s are denoted with white numbers and white arrows; diopside is labeled with black numbers and arrows in a white rectangle. Simulated diffraction patterns (DP) with indexing of both phases observed in the collected SAED pattern. Only α -cristobalite and diopside are shown for clarification in Fig. 2d, e, and f, respectively. Spots which appear in the α-cristobalite SAED pattern (001, 002, 003) are labeled as X's in the simulated DP (Fig. 2e, f). These are typically at extinction due to screw axis (4_1) but appear due to multiple diffraction effects.

Composition is straightforward. The silica precipitate EDS spectrum displays only silicon and oxygen peaks (Fig. 2c). Both the TEM images and the SAED pattern reveal homogeneous pyroxene structure with *C2/c* symmetry. Ordered omphacite lamellae (*P2/n* symmetry) known to occur in clinopyroxene structures were not observed. In addition, nano-scale amphibole occurs at the α-cristobalite interface; the crystals display excellent pyroxene/amphibole lattice matching (Fig. 2g). In this HRTEM lattice image of all three phases, the cristobalite can be seen in the midst of transforming to an amorphous phase as a result of damage from the electron beam. This happened more quickly at the amphibole/pyroxene interfaces, where no cristobalite lattice can be observed. In Fig. 2a, a planar boundary marked (101)α is observed in the cristobalite and explained in Fig. 3, where black arrows denote the location of the boundary in (a-c). Boxes denote areas of Fast Fourier Transform (FFT) patterns (Fig. 3c) on either side of the boundary in the HRTEM lattice image (Fig. 3a) and demonstrate that the planar boundary is the cristobalite twin plane (101). The amphibole and host diopside are labeled in (a) for reference. A schematic representation of the α-cristobalite lattice with twinned unit cells outlined in black (b) shows the near-perfect lattice fit on either side of the composition plane.

A second category of siliceous precipitates are non-crystalline Al-bearing silicate phases enclosed by the euhedral negative pyroxene shape. They are quite common; a select four are shown in Fig. 4. Dominant euhedral CPX planes are sharp and clear; however, SAED patterns from precipitates (e.g., Fig. 4b) generally show diffuse rings indicative of amorphous phases. A ring with weak intensity and some possible diffraction spots are attributed to crystallites of an unidentified mineral that was quickly destroyed by the electron beam. There is no other evidence of this mineral. The only chemical constituents observed via EDS (Fig. 4c) are Si, O, and Al. Al/Si ratios in the exsolved silica in Fig. 4 (as shown by EDS) range from 0.1 to 0.2. Preferential loss of alkali elements and low-atomic-number elements, such as Na and K, and during analytical electron microscopy gives rise to characteristically low count rates for those elements. In addition, with a focused probe for X-ray analyses such as used in this investigation, the damage rate to the sample is exacerbated by a high current density and results in the loss of these elements during X-ray collection (Ma et al. 1998). No amphiboles (or other H_2O-rich phases) are observed in the non-crystalline silica in Fig. 4, unlike the cristobalite or the third category of siliceous precipitates, which is non-crystalline, but also possesses amphibole (Fig. 5).

This group of siliceous phases (Fig. 5(a)) possess very similar features to the non-crystalline siliceous phases in Fig. 4, with one main difference: the presence of amphibole at the pyroxene/silica interface. Fig. 5 shows one of the siliceous, Al-bearing glass phases with amphibole. The EDS spectrum (c) displays an Al peak as in the non-crystalline phase in Fig. 4. Euhedral negative pyroxene morphology of the silica is still observed here, and, although the SAED pattern (Fig. 5d) shows this image is oriented at $[T01]_{Di}$, at an angle to CPX c-axis, the interface between diopside and the amphibole precipitate can still be seen to be coherent. Broad diffuse rings are observed in the silica SAED pattern (Fig. 5b), establishing that the silicate is

amorphous. White arrows in this SAED pattern point to a distinct faint ring representative of multiple small crystals. The extremely weak diffraction ring likely stems from the minerals indicated by black arrows in the white precipitate center (Fig. 5a). Identity of these minerals is unknown as they quickly disappeared under the energy of the electron beam. Inspection of the CPX/amphibole interface (Fig. 5e) illustrates the excellent lattice matching between the single and double chain silicates, and FFT patterns of both minerals further detail their crystallographic relationship: $[T01]_{Di} \parallel [100]_{Amp}$. A chemical formula calculated from the EDS spectrum using Cliff-Lorimer-based *k*-factors (Fig. 5f). This formula confirms a sodic-calcic amphibole (OH is assumed, not measured by EDS):

$$Na_{0.64}(Na_{0.26}Ca_{1.64}Fe_{0.10})(Mg_{3.06}Fe_{0.99}Al_{0.95})(Si_{6.68}Al_{1.32})O_{22}(OH)_2.$$

It is also of note that multiple crystals of phyllosilicates were observed in close proximity to some siliceous precipitates (Fig. 6a, b) in this investigation. In these precipitates, the shape of the non-pyroxene crystals is modified from the typical euhedral 'negative' pyroxene shape, with the sheet silicates fully covering the siliceous phase (Fig. 6a), but not the pyroxene. Dominant pyroxene planes, specifically {010} and {110} are highly degraded and the familiar euhedral negative pyroxene shape is unrecognizable. The composition (EDS spectrum taken from the area in (b)) is that of a talc-like phyllosilicate with ~9 Å (001) lattice fringes (Fig. 6c), and the SAED pattern (e) confirms pyroxene plus diffraction rings from multiple talc-like crystals.

Electron microprobe results

Table 1 presents recalculated electron microprobe (EMPA) data from a representative clinopyroxene grain in the Bohemian Massif eclogite. All clinopyroxenes analyzed via EMPA exhibit silica precipitates in their cores. Standard deviation and standard error of these data are

reported (SDEV= Standard deviation, SERR=Standard error, and n=17). Oxygen was calculated, not measured, and all calculations are normalized to six O atoms.

Almost all CPX analysis locations show sufficient Al to fill ^{IV}Al, the rest fills ^{VI}Al. The clinopyroxene is highly calcic (~Di_{68}, between diopside and omphacite), with very little to no K. UHP (non-stoichiometric) clinopyroxenes are characterized by significant cation deficiencies, with cations equaling <4 total cations/6 oxygen; this has been well-established in the literature (Smyth 1980; McCormick 1986; Proyer et al. 2004; Day and Mulcahy 2007; Konzett et al. 2008b; Zhao et al. 2011). Here, we broadly constrain possible vacancy content in clinopyroxene grains by assuming cation deficiencies exist in the structure as vacancies (cations + vacancies = four). Iron was measured via EMPA, and structural formula calculations involving only Fe^{2+} resulted in cations sum to ~ 4 or even slightly larger than 4, permitting no possible calculation of potential vacancy content. natural UHP clinopyroxenes, it is highly unlikely that all iron is Fe^{2+}, and some usefulness is found in estimating some amount of Fe^{3+} (Deer et al 1966) to calculate formulae. In general, Fe^{3+} is not measured, it is estimated by charge balance; in fact, these authors found no instances of measured Fe^{3+} data for the Nové Dvory eclogitic clinopyroxenes. A comparable UHP clinopyroxene bulk composition was found in another UHP regime—the Norwegian UHP clinopyroxenes of the Hareitland eclogite possess extremely similar bulk clinopyroxene compositions. Calculated Fe^{3+} data from Mysen (1972) show 1.1-1.7 wt. % Fe^{3+} in the Hareitland eclogitic clinopyroxenes. Utilizing this as a proxy and making the assumption that 2% of the total iron was Fe^{3+} in the UHP Nové Dvory clinopyroxenes, we tabulate both measured Fe^{2+} and assumed 2% Fe^{3+} amounts in Table 1. The host pyroxene is close to stoichiometric.

DISCUSSION

The occurrence of α-cristobalite and Na-Al-bearing silicate glass in UHP pyroxene raises several questions. First, did the cristobalite form as β-cristobalite (as commonly happens) and transform to α-cristobalite? Secondly, did the cristobalite form within its own range of metastability (~200-275 °C (Hatch and Ghose 1991)) or at UHP pyroxene stability? Thirdly, we interpret both the silica glass and α-cristobalite, which exhibit similar morphology, as primary exsolution phases—what mechanism may have formed these low-density phases, and is the same mechanism responsible for both?

Crystallographically-oriented silica in clinopyroxene from high- and ultrahigh-pressure pyroxenes, such as that investigated here, is widely interpreted to be the result of a complex combination of rock bulk composition, *P*, and *T* with a generally-accepted exsolution mechanism of excess silica from host clinopyroxene during decompression via the reaction:

$$2Ca_{0.5}\square_{0.5}AlSi_2O_6 = CaAl_2SiO_6 + 3SiO_2 + \square$$

($Ca_{0.5}\square_{0.5}AlSi_2O_6$= CaEskola (CaEs) vacancy solid solution in pyroxene, and □ = vacancy)

(Smyth 1980; Liou et al. 1998; Katayama et al. 2000; Dobrzhinetskaya et al. 2002; Klemd 2003; Zhang et al. 2005; Konzett et al. 2008a; Zhao et al. 2011). Substitution of CaEs component into pyroxenes results in non-stoichiometry, and pyroxene may then dissolve excess silica charge balanced by vacancies in M sites (Wood and Henderson 1978). Day and Mulcahy (2007) document clear evidence that vacancy consumption in non-stoichiometric clinopyroxene can release free silica. Vacancies are not the only way to result in pure silica from pyroxenes. Smith (2006) demonstrates that it is also theoretically possible to exsolve pure SiO_2 from non-stoichiometric pyroxene other than by the CaEs formula mechanism and leave behind

stoichiometric compositions. However, the non-stoichiometric character of HP/UHP clinopyroxene is well-established (Smyth 1980; McCormick 1986; Proyer et al. 2004; Day and Mulcahy 2007; Konzett et al. 2008b; Zhao et al. 2011), and we can conclude with some confidence that vacancies were most likely present in the UHP pyroxenes of the Bohemian Massif eclogite prior to decompression. These mechanisms produce silica irrespective of silica polymorph, and exsolution may not produce and maintain α-cristobalite and Na-Al-silicate glass phases to the exclusion of other silica polymorphs. Exsolution of excess silica from non-stoichiometric pyroxenes is merely the beginning of the answer, and formation of these unusual phases is likely an intricate combination of many processes.

In addition to excess silica, evidence of hydroxyl (water) observed in this investigation may play a part in the vacancy content and the particular polymorph exsolved in the CPX structure. Experimental studies have documented the incorporation of varying amounts of hydroxyl in synthetic clinopyroxene (Skogby and Rossman 1989; Skogby 1994), as well as natural clinopyroxenes (Skogby et al. 1990; Smyth et al. 1991; Bell et al. 1995; Koch-Muller et al. 2004; Katayama et al. 2006). It is reasonable to assume that OH was present in Nové Dvory clinopyroxenes. Observed micro- and nano-scale amphiboles are evidence of at least a sufficient amount of OH to transform clinopyroxene to amphibole, and to produce a siliceous melt during expulsion of excess silica and OH. Smyth et al. (1991) found a positive correlation between hydroxyl content and cation vacancy concentration in pyroxene from mantle-derived eclogite in the Roberts Victor kimberlite pipes. Katayama and Nakashima (2003) reported water contents as high as 3000 ppm in omphacite within a diamond-grade eclogite from the Kokchetav massif, Kazakhstan, although they assert this could be overestimated as much as 30%. Much lower OH

quantities are also known—31-60 ppm in diamond-bearing eclogite xenoliths of the Mir kimberlite pipe (Koch-Müller et al. 2004).

Cristobalite and silicate glass

High- (or β-) cristobalite is the stable low pressure polymorph of SiO_2 between 1470°C and its anhydrous melting point at~1728°C, but exists in a metastable form down to ~275°C. There, it undergoes a rapid and reversible displacive transition to the metastable phase α- (low-) cristobalite (Hatch and Ghose 1991). Beta-cristobalite is cubic (denoted below as subscript 'c') ($Fd\bar{3}m$); α-cristobalite is tetragonal ($P4_12_12$).

Metastable silica phases are not uncommon in nature, and cristobalite can be found in a variety of volcanic and metamorphic environments. Low- (or, α-) cristobalite is often found in volcanic ejecta, lunar rocks and meteorites due to quenching (Christie et al. 1971), and metastable cristobalite can also crystallize authigenically within sedimentary deposits as opal-CT (Jones and Segnit 1971). Planar boundaries and microstructures within cristobalite are physical evidence of the β→α transition. Microstructures in α-cristobalite following the β→α transition are well documented by Hatch and Ghose (1991), and via electron microscopy (Lally et al. 1978). None of these β→α transformation microstructures described above are observed in Fig. 2, indicating that this silica polymorph may have formed as α-cristobalite, not the expected higher density polymorphs coesite or quartz previous researchers have reported in UHP clinopyroxenes. Although none of the above transformation microstructures were observed in the Nové Dvory clinopyroxene, a single planar boundary along (101) in the α-cristobalite crystal is observed in Fig. 2. Planar boundaries along $(10l)_t$ have been observed in previous studies (Withers et al. 1989), but the exact nature of these boundaries and their relationship with β-

cristobalite is still unclear. Diopside surfaces likely served as sites for heterogeneous nucleation and epitaxial growth of cristobalite. Although there is evidence for the (101) boundary to be interpreted as a growth twin, it is possible this may be an inherited twin (not a transformation twin) from the β-phase (Lemmens et al. 2000). Thus, we cannot rule out the possibility that the cristobalite transformed from the high temperature β- to α- cristobalite. It may be that the crystal is simply too small to display all of the transformation microstructures typical of this transformation.

Silicate glass can be found in many environments. Nanometer-size P/K-rich silica glass inclusions are found in microdiamond from gneisses of the Kokchetav and Erzgebirge massifs (Hwang et al. 2006). These are interpreted as former melt inclusions that reflect the chemical character of their host rocks and may have been generated through partial melting of gneissic rocks and/or dehydration/decarbonation processes in marble (Hwang et al. 2006). Pertinent to this investigation, highly silicic glass inclusions are found commonly present in Mg-rich minerals (olivine and pyroxene) of xenolithic terrestrial upper mantle rocks and have many similarities with glass inclusions from mafic minerals of achondritic meteorites (Varela et al. 1998).

Mechanisms of formation—silicate glass

As shown above, the non-stoichiometric character of UHP clinopyroxene has been well-established. If exsolution of excess silica is intimately linked to the non-stoichiometry of UHP clinopyroxene, it is possible that both non-crystalline Al-bearing silicate phases and α-cristobalite nucleated and exsolved from Ca-Es-bearing clinopyroxene. Simultaneous expulsion of OH held within the clinopyroxene structure at high temperatures most likely caused the partial

melting of silica that created Na-Al-silicate glass phases, and growth of amphiboles associated with α-cristobalite. It is at this point in the story that formation mechanisms of α-cristobalite and silica glass diverge slightly.

We propose that the glass precipitates in this study (Figs. 4, 5) are likely formed through partial melting of the silica and albite components, as silica, a jadeite component, and OH are expelled from the pyroxene lattice. Although silica-rich, aluminous alkali-rich glasses have been found in Mg-rich minerals of both terrestrial upper mantle rocks and achondrites, mechanisms of formation in the two cases are different. Varela et al. (1997) observed that although many processes were likely to have contributed to their formation— low-degree partial melting, precipitation from silicate-loaded fluids, fractional crystallization and liquid immiscibility, or residual glass from a parent magma—glass inclusions in olivine and pyroxene of upper mantle peridotites were more likely related to a very low degree of partial melting. Precipitation from silicate-loaded fluids can be ruled out in the formation of glass in the Nové Dvory eclogite and garnet pyroxenite, as it is more often associated with fractures and cross-cutting grain boundaries that suggest migration of fluids through the grain, not isolated precipitation in cores of grains. And, as can be seen in Fig. 1, the cores of clinopyroxenes in the rock are quite fresh, without obvious subsequent alteration. Fractional crystallization and liquid immiscibility may be ruled out on the basis that this phenomenon is typically extremely FeO-rich and, with these compositions, is generally found in lunar environments. Table 1 compositions show these pyroxenes possess some FeO,but may not be enriched enough for that. Residual glass from a parent magma can also be ruled out. Varela et al. (1997) state that silica-rich glass inclusions in upper mantle xenoliths are incompatible with this genesis, as residual melts that form glass likely represent independent components trapped during crystallization of primary magma components.

Although Na is not observed now as it disappears quickly under the electron beam and can be difficult to capture, the potential presence of Na allows for us to consider the Al-bearing glass as a mixture of albite and silica components in a silica-albite eutectic system. The calculated range of Al/Si ratios (0.1-0.2) from the glasses is close to the eutectic composition in the $NaAlSi_3O_8$-SiO_2-H_2O (Ab + Qz + H_2O) system—at 0.1 GPa and 800 °C (Wen and Nekvasil 1994). The eutectic temperature at low pressures is similar for hydrous versus anhydrous conditions—at 1 bar, the temperatures of the eutectics are shown to be 1007 °C and 1009 °C, respectively. In a H_2O-saturated system, which is not the case here, an increase in pressure causes the temperature of the eutectic to drop—at 7 kbar, the eutectic is 682 °C. In an anhydrous system, a pressure increase to 7 kbar causes the eutectic temperature to increase dramatically to 1132 °C, and at 15 kbar (1.5 GPa), the eutectic moves to 1228 °C. Calculated *P-T* estimates of the UHP mantle garnet peridotite which hosts the thin layers of the Nové Dvory eclogite are 875–1150 ºC, 33–60 kbar (Medaris et al. 2006). At our calculated Al/Si ratio range of 0.1-0.2, the temperature of the eutectic in an anhydrous system which is similar to a hydrous system, as mentioned above, (at 5 kbar) is ~1100°C, as shown by Wen and Nekvasil (1994). This temperature is possible for glass formation. Figure 8 is a diagram illustrating the pressure difference between the precipitates (curve c) and the host minerals (curve b). Melt inclusions will be over-pressured (curve a) with respect the host mineral and precipitates will be under-pressured with respect to the host mineral.

It is unlikely that the glass-forming components (jadeite component, silica, vacancy, and OH) were expelled from the clinopyroxene lattice at peak metamorphic *P-T*. Rather, they may have been expelled at varying high temperatures post-metamorphic peak during decompression, when these elements formed a melt at the eutectic. In fact, modeling of thermal boundary conditions of exhumation rates in UHP rocks has shown that in the absence of lateral heating,

rocks exhuming from great depth always cool or decompress isothermally, and the main cooling period at shallower crustal levels follows the main period of exhumation (Grasemann et al. 1998). We may use the modeling results of Grasemann et al (1998) to propose that a glass formed at the eutectic in the Ab + Qz + (low) H_2O system with an Al/Si ratio of 0.1-0.2 may have formed at many different depths along the exhumation pathway. To narrow the temperature range in which the glass formed, we must also consider contributing factors that likely lowered the temperature at which the melt can form. See the section entitled "*Contributing factors that aid in α-cristobalite and silica glass formation"* for a discussion of these factors.

Mechanisms of formation—α-cristobalite

The key to a-cristobalite formation may the stability of the CPX lattice during subduction and exhumation. Metastable cristobalite has previously been found in high pressure garnet granulite from Gore Mountain, New York. This cristobalite within garnet likely originated as small trapped samples of hydrous Na-Al-siliceous melt where diffusive loss of water from the inclusions under isothermal, constant volume conditions may have resulted in a large enough internal pressure decrease to promote the metastable crystallization of cristobalite (Darling et al. 1997). In the Nové Dvory eclogite as in the Gore Mountain garnet, a crystal may form under constant volume conditions due to the high tensile strength and low thermal expansivity/compressibility of diopside compared with α-cristobalite (Berman 1988). No evidence of volume change is observed in the Nové Dvory clinopyroxenes in optical (Fig. 1) or HRTEM (Fig. 2) micrographs as a result of silica polymorphic transformations or changes in density from host clinopyroxene (~3.3 g/cm^3) to cristobalite (2.32 g/cm^3). Darling et al. (1997)

attribute formation of low pressure cristobalite to an open system in which mass is removed from the system, causing lowered pressure. We hypothesize a locally-closed system at the point of silica exsolution in the case of the α-cristobalite crystal in Fig. 2. Exsolution of vacancies (assumed density of ~0.0 g/cm^3) that coalesce may cause a void and aid in this localized density decrease. The density of the surrounding pyroxene (~3.3 g/cm^3) minus precipitated α-cristobalite (2.32 g/cm^3) plus a potential coalesced vacancy void (0.0 g/cm^3) is a negative change of ~ 1 g/cm^3 . An arrow in Fig. 2 points to a potential void at the interface of silica and pyroxene. We interpret this as an area of expelled, coalesced vacancies. If we interpret Fig. 2 in such a way as to assume overall volume is preserved in clinopyroxene during silica exsolution, and assume simultaneous vacancy expulsion and coalescence, a low pressure micro- or nano-environment may be generated at any depth in response to density changes, perhaps via a reaction similar to this:

$$2Mg_{1.5}\,\square_{0.5}\,Si_2O_6H \rightarrow 1.5Mg_2Si_2O_6 + \square + SiO_2 + H_2O$$

Vacancies are point defects in the crystal structure that create non-stoichiometry and are also notoriously difficult to image with the TEM. We can assume the unstable vacancies have been expelled from the destabilized pyroxene lattice and cannot be imaged in situ. Fortunately, cases exist in which point defects form clusters and have been imaged readily with TEM methods (Veblen and Cowley 1994). We believe this may be the mechanism which aids in forming a low pressure micro-environment. As in the case of the Gore Mountain garnet, this interpretation requires that the host mineral (clinopyroxene) maintain a pressure differential between the small inclusions and the outside of the clinopyroxene. This pressure differential, in addition to the high tensile strength and low thermal expansivity/compressibility of the clinopyroxene (Berman 1988) likely serves to preserve micro- and nano-scale stable and

metastable minerals within the clinopyroxene during exhumation. Results of recent synthetic fluid inclusion studies on quartz demonstrate that high pressure differences can be maintained over small distances at high temperatures in cases where the internal inclusion pressure is lower than external confining pressure (Sterner and Bodnar 1989; Vityk et al. 1995). In this way, metastable phases such as α-cristobalite and the siliceous non-crystalline phases may persevere to the surface from any depth.

This mechanism has been used by these authors (Hill et al, 2013) to explain another instance of silica exsolution from UHP diopside in the Kokchetav Massif. In this diopside, low-pressure keatite with accompanying amphibole was identified, also with no evidence of volume change within the clinopyroxene crystal. Formation of α-cristobalite is favored over keatite in the Nové Dvory eclogite as a result of higher temperatures than Kokchetav Massif garnet pyroxenite.

Contributing factors that aid in α-cristobalite and silicate glass formation

Although it appears likely that both α-cristobalite and silica glass initiated formation in a similar manner, the crystalline nature of α-cristobalite requires a different formation environment than glass. Already discussed is the low-pressure micro-environment that may have been produced by vacancy expulsion/coalescence and subsequent density decrease under constant volume conditions, thus creating a suitable *P* and *T* for α-cristobalite. A number of other factors may have contributed to the formation of metastable α-cristobalite.

Favorable interface energy due to excellent lattice matching and nano-scale size effects may have played integral parts in lowering the nucleation and crystallization energy. Generation/exsolution of metastable phases takes place when the kinetically-preferred path

differs from the preferred thermodynamic path (Baricco et al. 2004). In this way, exsolution of a metastable phase may be preferred over a more stable phase. Mineral nano-particles commonly behave differently as a function of their size within the nano-scale range. Mineral nano-particles also behave differently than larger micro- and macroscopic crystals of the same structure and composition. At the nano-scale, three factors compete to stabilize a given polymorph: enthalpy of polymorphic transition, surface enthalpy, and enthalpy of hydration (Barnard and Xu 2008; Hochella et al. 2008). Navrotsky et al. (2004) reported that competition between surface enthalpy and the energetics of phase transformation leads to the general conclusion that polymorphs that are metastable as micron-sized or larger crystals can often be thermodynamically stabilized at the nano-scale. Nanocrystals of protoenetstite within plagioclase are quenchable and stable at low-temperature (Xu et al. 2017a). This phenomenon has been observed in TiO_2 polymorphs, aluminum and iron oxides, and oxyhydroxides (Navrotsky 2003; Navrotsky et al. 2004; Chen and Fu 2006; Barnard and Xu 2008; Navrotsky et al. 2009; Lee and Xu 2016; Lee et al. 2016). Thus, we infer metastable nano-scale α-cristobalite may be stabilized in part due to its small size.

Additionally, the size at which a nano-scale mineral forms/melts is temperature dependent. Extensive research has shown that decreasing particle size also decreases the temperature at which the particle forms (Barnard and Xu 2008; Barnard et al. 2009). This melting/crystallization point depression occurs for nearly all free nanoparticles, e.g. Au, TiO_2, Pt (Barnard et al. 2009; Barnard et al. 2011), and for some nano-particles embedded in a matrix. Melting point depression is also observed as a function of dimension (Zhang et al. 2000).

The melting point depression can be dramatic. As the particle shrinks to the nanoscale, the interfacial energy (γ) penalty becomes significant when compared to total bulk energy (ΔH).

This, in turn, destabilizes the particle with respect to the melt (DeHoff 2006). Assuming an l x l x 3l rectangle particle shape as observed in TEM (Fig. 4), this destabilizing effect for a pure silica glass results in nearly a 300˚C melting temperature depression for an l = 50 nm particle as the melting temperature drops from 1723˚C to 1430˚C. The same calculations for l = 100 and 200 nm yield a 140˚C and 70˚C depression, respectively:

$$\lambda_m = \frac{3\gamma\, M}{\rho_s\, \Delta \mathrm{H}} \qquad (1)$$

$$T_m(\ell) = T_m(\infty)\left[1 - \lambda_m \frac{1}{\ell}\right] \qquad (2)$$

where, l (length), γ (interfacial energy) = 4.4 J/m^2, M (molar mass) = 60.08 g/mol, p_s (density) = 2.203E6 g/m^3, $T_m(\infty)$ = 1996 K (1723˚C), ΔH (bulk enthalpy of fusion) = 50.55 kJ/mol

In combination with nano-scale size effects, mechanisms of exsolution are closely related to the types of interfaces that develop between two phases. The geometry of the substrate in epitaxial mineral growth is known to cause growth of phases not stable at existing *P*-*T*-X conditions. The morphology of silica glass and α-cristobalite is certainly dominated by the clinopyroxene lattice (Figs. 2, 4, 5), and a high degree of lattice match between the two likely serves to stabilize the nano-scale α-cristobalite crystal. The structural relationship of α-cristobalite with diopside derived from the SAED pattern (Fig. 2a) is schematically-represented in Fig. 7. In all models $[001]_{CPX} \parallel [010]_{\alpha\text{-cristobalite}}$. Here we show $(010)_{CPX} \sim \parallel (-101)\alpha$ (Fig. 7a) and $(\bar{1}\bar{1}0)_{CPX} \sim \parallel (100)\alpha$ (Fig. 7b). These models illustrate that diopside and silica lattices join with little to no bending of the silica tetrahedra. Diopside (010) is parallel to α-cristobalite $(\bar{1}01)$, and Fig. 7d illustrates the close lattice match with unit cell dimensions: d_{100} of diopside is 9.3 Å, while α-cristobalite d_{101} 4.04 Å. This is a mere 5% difference over just two unit cells of diopside

and three unit cells of α-cristobalite, where $5d_{101\alpha}$ (5 x 4.04 Å) is approximately equal to $2d_{100CPX}$ (2x9.3 Å). In addition, very minor mismatch between α-cristobalite and diopside likely minimizes the nucleation energy which aids a favorable configuration of silica tetrahedra.

The presence of amphibole in association with α-cristobalite and some glass precipitates may be a clue to localized water quantities. Silica glass exsolution with amphibole may have formed below the eutectic temperature and at a later stage than glass precipitates without amphibole. Nano-crystals of α-cristobalite plus amphibole likely possessed less localized water than the glass precipitates and may have formed after glass precipitates with and without amphibole. The amphibole in Fig. 3 appears to have been encompassed by the exsolving silica rather than transforming from pyroxene along the edge. A possible explanation is that the diopside expelled only a small amount of water at this locality and only a nano-scale portion of the pyroxene rehydrated to amphibole.

In this paper, we propose that the unique properties of HP/UHP pyroxenes discussed above (excess silica balanced by structural vacancies, OH held within the lattice and expelled during precipitate formation) drive exsolution from the clinopyroxene structure and form silicate minerals and melts. In addition, we interpret the silicate glass Al/Si ratios of 0.1-0.2 to correlate well with Al-bearing silicate glasses forming from a siliceous melt at high temperature on the eutectic in the Ab-Qz-H_2O system. a slightly later stage and lower temperature, the metastable low density silica polymorph α-cristobalite nucleated on diopside planes that served as sites for solid state heterogeneous nucleation and epitaxial growth. Assuming that the pyroxene (a stable crystal) has not experienced volume change at the point of low density silica exsolution, a metastable phase may form and persist within the host due to an internal pressure decrease.

Thus, a low pressure micro-environment may be created at the point of low density cristobalite formation.

Later stage alteration of silica precipitates

Some silica precipitates in this investigation are observed to have altered to talc-like phyllosilicates (Fig. 6). This appears similar to exsolved silica altered to high-silica sheet silicates from UHP clinopyroxene of the Kokchetav Massif (Hill et al. 2013). Here, as in the Kokchetav Massif, the dominant planes of the euhedral clinopyroxene have degraded and are nearly unrecognizable (Fig. 6a). Multiple crystals of sheet silicates in random orientation show a composition that is unexplainably high in silica (Fig. 6c), where no silica precipitate is observed. Due to the similarities of the two cases, we continue to interpret the sheet silicates as a later stage alteration of silica by replacement reaction due to fluid migration, similar to the results of Dobrzhinetskaya et al. (2009), localized on silica during rock retrogression. Refer to Hill et al. (2013) for a more detailed explanation.

IMPLICATIONS

Nano-scale investigation of formation processes of precipitates of silicate glass and cristobalite / amphibole intergrowths in UHP pyroxene may be important to help us better understand OH (or water) in eclogitic host pyroxene during subduction, and its ultimate release in the mantle. As geologists have little access to minerals from UHP terranes to study, the findings here have great significance for investigation of rocks that weren't commonly believed to exist a mere 20-30 years ago. This study revealed vacancies and OH in high-pressure pyroxene that formed during subduction. When the host rock is exhumed, the incorporated OH

migrates out from the UHP pyroxene structure together with vacancies and excess silica in multiple forms of glass and cristobalite / amphibole precipitates. If the pyroxene-bearing slab subducts further into the mantle, the pyroxene may release the incorporated OH into mantle during its phase transformation to garnet and/or perovskite structures. The subsequent effects on mantle rocks are worthy of investigation.

Characterization of nano-scale phases inside UHP rocks is also significant for understanding the larger scale geodynamics of collisional terranes, particularly when unexpected (metastable) phases make an appearance. Geologic processes occurring deep in the Earth and under UHP conditions are difficult to recognize due to subsequent retrogressive reactions and fluid and deformation events experienced by rocks during exhumation. Only by identifying minerals and their mechanisms of exsolution at the nano-scale to track the path of these rocks can we understand in detail the processes operating deep in the Earth. Silica precipitates in Nové Dvory clinopyroxenes were previously thought to be quartz; however, our investigation reveals a variety of low pressure, high temperature, and/or metastable phases greatly affected by the presence of water in clinopyroxenes. The high tensile strength and low thermal expansivity / compressibility of diopside serves to preserve phases typically unlikely to make it to the surface without recrystallizing. When compared to observed silica phases, this may mean that the exsolved phases have little to no effect on the rheology of the exhuming rock but could affect the interpretation of the *P*-*T* path. Some low-density precipitates containing Na and K may be formed through similar precipitation processes, instead of melt inclusions. *P*-*T* evolution for the precipitates and inclusions are very different. The precipitates are under-pressured with respect to the host mineral. However, the melt inclusions are over-pressured.

REFERENCES CITED

Anderson, E. D. and Moecher, D. P. (2007). Omphacite breakdown reactions and relation to eclogite exhumation rates. Contributions to Mineralogy and Petrology, 154, 253–277.

Bakun-Czubarow, N. (1992). Quartz pseudomorphs after coesite and quartz exsolutions in eclogitic omphacites of the Zlote Mountains in the Sudetes (SW Poland). Archiwum Mineralogiczne, 48(1-2), 3-25.

Barnard, A. S., and Xu, H. (2008). An Environmentally Sensitive Phase Map of Titania Nanocrystals. ACS Nano, 2(11), 2237-2242.

Barnard, A. S., Konishi, H., & Xu, H. (2011). Morphology mapping of platinum catalysts over the entire nanoscale. Catalysis Science and Technology, 1, 1440-1448.

Barnard, A. W., Young, N. P., Kirkland, A. I., van Huis, M. A., & Xu, H. (2009). Nanogold: A Quantitative Phase Map. ACS Nano, 3(6), 1431-1436.

Baricco, M., Palumbo, M., Baldissin, D., Bosco, E., and Battezzati, L. (2004). Metastable phases and phase diagrams. La Metallurgia Italia, 11-12, pp. 1-8.

Bell, D., Ihinger, P. H., and Rossman, G. R. (1995). Quantitative analysis of trace OH in garnet and pyroxenes. American Mineralogist, 80, 465-474.

Berman, R. G. (1988). Internally-Consistent Thermodynamic Data for Minerals in the System Na_2O-K_2O-MgO-FeO-Fe_2O_3-SiO_2-TiO_2-H_2O-CO_2. Journal of Petrology, 29, 445-542.

Bi, H., Song, S., Dong, J., Yang, L., Qi, S., Allen, M. (2018). First discovery of coesite in eclogite from East Kunlun, northwest China. Science Bulletin, 63, 1536-1538.

Boettcher, A. L. and Wyllie, P. J. (1968). Jadeite stability measured in the presence of silicate liquids in the system $NaAlSiO_4$-SiO_2-H_2O. *Geochimica et Cosmochimica Acta*, *32*(9), 999-1012.

Brueckner, H.K., Medaris Jr., L. (1998). A tale of two orogens — the contrasting P–T–t history and geochemical evolution of mantle in ultrahigh pressure (UHP) metamorphic terranes of the Norwegian Caledonides and the Czech Variscides. Schweizerische Mineralogische und Petrographische Mitteilungen, 78, 293–307.

Brueckner, H.K., Medaris Jr., L.G., 2000. A general model for the intrusion and evolution of 'mantle' garnet peridotites in high-pressure and ultra-high pressure metamorphic terranes. Journal of Metamorphic Geology, 18, 123–134.

Burnham, C. W. and Davis, N. F. (1974). The role of H_2O in silicate melts; II, Thermodynamic and phase relations in the system $NaAlSi_3O_8$-H_2O to 10kilobars, 700 degrees to 1100 degrees C. *American Journal of Science*, *274*(8), 902-940.

Carswell, D., and O'Brien, P. J. (1993). Thermobarometry and geotectonic significance of high-pressure granulites. Examples from the Moldanubian Zone of the Bohemian Massif in lower Austria. Journal of Petrology, 34, 427-459.

Carswell, D., van Roermund, H. L., and Wiggers de Vries, D. (2006). Scandian ultrahigh-pressure metamorphism of Proterozoic basement rocks on Fjortoft and Otroy, Western Gneiss Region, Norway. International Geology Review, 48, 957-977.

Chen, J., and Fu, Z. (2006). α-PbO2-type nanophase of TiO_2 from coesite-bearing eclogite in the Dabie Mountains, China. Comment. American Mineralogist, 91, 1699-1700.

Chopin, C. (1984). Coesite and pure pyrope in high-grade blueschists of the Western Alps: a first record and some consequences. Contributions to Mineralogy and Petrology, 86, 107-118.

Christie, J., Lally, J. S., Heuer, A. H., Fisher, R. M., Griggs, D. T., and Radcliffe, S. V. (1971). Comparative electron petrography of Apollo 11, Apollo 12, and terrestrial rocks. Proceedings of the Second Lunar Science Conference. Supplement 2, p. 69. Geochimica et Cosmochimica Acta.

Coleman, R., and Wang, X. (1995). Ultrahigh Pressure Metamorphism. New York: Cambridge University Press.

Cooke, R., O'Brien, P. J., and Carswell, D. A. (2000). Garnet zoning and the identification of equilibrium mineral compositions in high-pressure-temperature granulites from the Moldanubian Zone, Austria. Journal of Metamorphic Geology, 18, 551-569.

Darling, R. S., Chou, I.-M., and Bodnar, R. J. (1997). An Occurrence of Metastable Cristobalite in High-Pressure Garnet Granulite. Science, 276, 91-93.

Day, H., and Mulcahy, S. R. (2007). Excess silica in omphacite and the formation of free silica in eclogite. Journal of Metamorphic Geology, 25, 37-50.

Deer, W., Howie, R. A., & Zussman, J. (1966). An introduction to the Rock-forming Minerals. London: Longman.

DeHoff, R. (2006). Thermodynamics in Materials Science. New York: Taylor & Francis Group.

Dobrzhinetskaya, L. F., Eide, E. A., Larsen, R. B., Sturt, B. A., Tronnes, R. G., Smith, D. C., et al. (1995). Microdiamond in high-grade metamorphic rocks of the Western Gneiss Region, Norway. Geology, 2, 597-6000.

Dobrzhinetskaya, L. F., Wirth, R., and Green II, H. W. (2006). Nanometric inclusions of carbonates in Kokchetav diamonds from Kazakhstan: a new constraint for the depth of their origin. Earth and Planetary Science Letters, 243, 85-93.

Dobrzhinetskaya, L. F., Wirth, R., Rhede, D., Liu, Z., and Green, H. W. (2009). Phlogopite and quartz lamellae in diamond-bearing diopside from marbles of the Kokchetav massif, Kazakhstan: exsolution or replacement reaction? Journal of Metamorphic Petrology, 27, 607-620.

Dobrzhinetskaya, L., Schweinehage, R., Massonne, H. J., and Green, H. W. (2002). Silica precipitates in omphacite from eclogite at Alpe Arami, Switzerland: evidence of deep subduction. Journal of Metamorphic Geology, 20, 481-492.

Dokukina, K. A. and Konilov, A. N. (2011). Metamorphic evolution of the Gridino Mafic Dyke Swarm (Belomorian Eclogite Province, Russia). In L. F. Dobrzhinetskaya, S. W. Faryad, & S. Wallis (Eds.), Ultrahigh-pressure metamorphism. 25 years after the discovery of coesite and diamond (pp. 579–621). London: Elsevier.

Ducea, M., and Saleeby, J. (1998). Crustal recycling beneath continental arcs: silica-rich glass inclusions in ultramafic xenoliths from the Sierra Nevada, California. Earth and Planetary Science Letters, 156, 101-116.

Faryad, S. W. and Fisera, M. (2015). Olivine-bearing symplectites in fractured garnet from eclogite Moldanubian zone (Bohemian massif) – A short-lived, granulite facies event. Journal of Metamorphic Geology, 33, 597–612.

Gayk, T., Kleinschrodt, R., Langosch, A., and Seidel, E. (1995). Quartz exsolution in clinopyroxene of high-pressure granulite from the Munchberg Massif. European Journal of Mineralogy, 7, 1217-1220.

Grasemann, B., Ratschbacher, L., and Hacker, B. R. (1998). Exhumation of Ultrahigh-Pressure Rocks: Thermal Boundary Conditions and Cooling History. In B. R. Hacker, and J. G. Liou (Eds.), When Continents Collide: Geodynamics and Geochemistry of Ultrahigh-Pressure Rocks, p. 117-139. The Netherlands, The Netherlands: Kluwer Academic Publishers.

Hatch, D. M., and Ghose, S. (1991). The alpha to beta Transition in Cristobalite, SiO_2: Symmetry Analysis, Domain Structure, and the Dynamical nature of the beta-phase. Physics and Chemistry of Minerals, 17, 554-562.

Hill, T. R., Konishi, H., and Xu, H. (2013). Natural occurrence of keatite precipitates in UHP clinopyroxene from the Kokchetav Massif: a TEM investigation. American Mineralogist, 98, 187-196.

Hochella, J. M., Lower, S. K., Maurice, P. A., Penn, R. L., Sahai, N., Sparks, D. L., et al. (2008). Nanominerals, Mineral Nanoparticles, and Earth systems. Science, 319, 1631-1634.

Hwang, S.-L., Chu, H.-T., Yui, T.-F., Shen, P., Schertl, H.-P., Liou, J. G., et al. (2006). Nanometer-size P/K-rich silica glass (former melt) inclusions in microdiamond from the gneisses of Kokchetav and Erzgebirge massifs: Diversified characteristics of the formation media of metamorphic microdiamond in UHP rocks due to host-rock buffering. Earth and Planetary Science Letters, 243, 94-106.

Janak, M., Froitzheim, N., Luptak, B., Vrabec, M., and Krogh Ravna, E. (2004). First evidence for ultrahigh-pressure metamorphism of eclogites in Pohorje, Slovenia: tracing deep continental subduction in the eastern Alps. Tectonics, 23, 1-10.

Jones, J., and Segnit, E. R. (1971). The nature of opal. I. Nomenclature and constituent phases. Journal of the Geological Society of Australia, 18, 57-68.

Katayama, I., Parkinson, C., Okamoto, K., Nakajima, Y., and Maruyama, S. (2000). Supersilicic clinopyroxene and silica exsolution in UHPM eclogite and pelitic gneiss from the Kokchetav massif, Kazakhstan. American Mineralogist, 85, 1368-1374.

Katayama, I., and Nakashima, S. (2003). Hydroxl in clinopyroxene from the deep subducted crust; evidence for H2O transport into the mantle. American Mineralogist, 88, 229-234.

Katayama, I., Nakashima, S., and Yurimoto, H. (2006). Water content in natural eclogite and implication for water transport into the deep upper mantle. Lithos, 86, 245-259.

Katayama, I., Parkinson, C. D., Okamoto, K., Nakajima, Y., and Maruyama, S. (2000). Supercilicic clinopyroxene and silica exsolution in UHPM eclogite and pelitic gneiss from the Kokchetav massif, Kazakhstan. American Mineralogist, 85, 1368-1374.

Klemd, R. (2003). Ultrahigh-pressure metamorphism in eclogites from the western Tianshan high-pressure belt (Xinjiang, western China). American Mineralogist, 88, 1153-1156.

Koch-Muller, M., Matsyuk, S. S., and Wirth, R. (2004). Hydroxyl in omphacites and omphacitic clinopyroxenes of upper mantle to lower crustal origin beneath the Siberian platform. American Mineralogist, 89, 921-931.

Konilov, A. N., Shchipansky, A. A., Mints, M. V., Dokukina, K. A., Kaulina, T. V., Bayanova, T. B., Natapov, L.M., Belousova, E.A., Griffin, W.L., and O'Reilly, S. Y. (2011). The Salma eclogites of the Belomorian Province, Russia: HP/UHP metamorphism through the subduction of Mesoarchean oceanic crust. In L. F. Dobrzhinetskaya, S. W. Faryad & S.

Wallis (Eds.), Ultrahigh-pressure metamorphism. 25 years after the discovery of coesite and diamond (pp. 623–670). London: Elsevier.

Konzett, J., Frost, D. J., Proyer, A., and Ulmer, P. (2008a). The Ca-Eskola component in eclogitic clinopyroxene as a function of pressure, temperature, and bulk composition: an experimental study to 15 GPa with possible implications for the formation of oriented SiO_2-inclusions in omphacite. Contributions to Mineralogy and Petrology, 155, 215-228.

Konzett, J., Libowitzky, E., Hejny, C., Miller, C., and Zanetti, A. (2008b). Oriented quartz + calcic amphibole inclusions in omphacite from the Saualpe and Pohorje Mountain eclogites, Eastern Alps--An assessment of possible formation mechanisms based on IR- and mineral chemical data and water storage in Eastern Alpine eclogites. Lithos, 336-350.

Lee, S., and Xu, H. (2016) Size-dependent phase map and phase transformation kinetics for nanometeric iron(III) oxides (γ→ε→α pathway). The Journal of Physical Chemistry C, 120, 13316–13322.

Lee, S., Shen, Z. and Xu, H. (2016) Study on nanophase iron oxyhydroxides in freshwater ferromanganese nodules from Green Bay, Lake Michigan. American Mineralogist, 101, 1986-1995.

Lemmens, H., Czank, M., Van Tendeloo, G., Amelinckx, S. (2000). Defect structure of the low temperature α-cristobalite phase and the cristobalite ↔ tridymite transformations in (Si-Ge)O_2. Physics and Chemistry of Minerals, 27(6), 386-397.

Lally, J., Nord, G. L., Heuer, A. H., and Christie, J. M. (1978). Transformation-induced defects in α-cristobalite. Proceedings of the Ninth International Congress on Electron Microscopy, 1, p. 476-477.

Li, X., Zhang, L., Wei, C., Slabunov, A.I., and Bader, T. (2018). Quartz and orthopyroxene exsolution lamellae in clinopyroxene and the metamorphic P–T path of Belomorian eclogites. Journal of Metamorphic Geology, 36, 1-22.

Liou, J., Zhang, R. Y., Ernst, W. G., Rumble, D., and Maruyama, S. (1998). High-pressure minerals from deeply subducted metamorphic rocks. In R. Hemley (Ed.), Ultrahigh-pressure Mineralogy: Physics and Chemistry of the Earth's Deep Interior, 37, 33-96. Mineralogical Society of America.

Ma, C., FitzGerald, J., Eggleton, R., Llewellyn, D. (1998). Analytical electron microscopy in clays and other phyllosilicates: Loss of elements from a 90-nm stationary beam of 300-keV electrons. Clays and Clay Minerals. 46(3), 301-316.

Massonne, H.-J. (1998). A new occurrence of microdiamonds in the quartzofeldspathic rocks of the Saxonian Erzgebirge, Germany, and their metamorphic evolution. In J. Gurney, J. Gurney, and M. D. Pascoe (Ed.), Proceedings of the VIIth International Kimberlite Conference, 533-539.

Massonne, H.-J. (2001). First find of coesite in the ultrahigh-pressure metamorphic area of the central Erzgebirge, Germany. European Journal of Mineralogy, 13, 565-570.

Matte, P. (2001). The Variscan collage and orogeny (480-290 Ma) and the tectonic definition of the Armorica microplate: a review. Terra Nova, 13, 122-128.

McCormick, T. C. (1986). Crystal-chemical aspects of nonstoichiometric pyroxenes. American Mineralogist, 71, 1434-1440.

Medaris, J. G., Wang, H., Jelinek, E., Mihaljevic, M., and Jakes, P. (2005). Characteristics and origins of diverse Variscan periodites in the Gföhl Nappe, Bohemian Massif, Czech Republic. Lithos, 82, 1-23.

Medaris, J. L., Beard, B. L., and Jelinek, E. (2006). Mantle-Derived, UHP Garnet Pyroxenite and Eclogite in the Moldanubian Gfohl Nappe, Bohemian Massif: A Geochemical Review, New P-T Determinations, and Tectonic Interpretation. International Geology Review, 48, 765-777.

Mysen, B. (1972). Five Clinopyroxenes in the Hareidland Eclogite, Western Norway. Contributions to Mineralogy and Petrology, 34, 315-325.

Nakano, N., Osanai, Y., and Owada, M. (2007). Multiple breakdown and chemical equilibrium of silicic clinopyroxene under extreme metamorphic conditions in the Kontum Massif, central Vietnam. American Mineralogist, 92(11–12), 1884–1855.

Nakano, N., Osanai, Y., Owada, M., Nam, T. N., Toyoshima, T., Binh, P., Tsunogae, T., Kagami, H. (2007). Geologic and metamorphic evolution of the basement complexes in the Kontum Massif, central Vietnam. Gondwana Research, 12, 438–453.

Nanda, K. (2009). Size-dependent melting of nanoparticles: Hundred years of thermodynamic model. Pramana-Journal of Physics, 72(4), 617-628.

Navrotsky, A. (2003). Energetics of nanoparticle oxides: interplay between surface energy and polymorphism. Geochemical Transactions, 4(6), 34-37.

Navrotsky, A. (2004). Energetic clues to pathways to biomineralization: Precursors, clusters, and nanoparticles. Proceedings of the National Academy of Sciences, 101(33), 12096-12101.

Navrotsky, A, Mazeina, L. Majzlan, J. (2009). Size-driven Structural and Thermodynamic Complexity in Iron Oxides. Science, 319, 1635-1638.

Page, Z. F., Essene, E. J., and Mukasa, S. B. (2005). Quartz exsolution in clinopyroxene is not proof of ultrahigh pressures: Evidence from eclogites from the Eastern Blue Ridge, Southern Appalachians, U.S.A. American Mineralogist, 90, 1092-1099.

Proyer, A., Dachs, E., and McCammon, C. (2004). Pitfalls in geothermobarometry of eclogites: Fe^{3+} and changes in the mineral chemistry of omphacite at ultrahigh pressures. Contributions to Mineralogy and Petrology, 147, 305-318.

Proyer, A., Krenn, K., and Hoinkes, G. (2009). Orientated precipitates of quartz and amphibole in clinopyroxene of metabasites from the Greek Rhodope: A product of open system precipitation during eclogite-granulite-amphibolite transition. Journal of Metamorphic Geology, 27(9), 639–654.

Rampone, E., Morten, L. (2001). Records of crustal metasomatism in the garnet peridotites of the Ulten Zone (Upper Austroalpine, Eastern Alps). Journal of Petrology 42/1, 207–219.

Sajeev, K., Kawai, T., Omori, S., Windley, B. F., and Maruyama, S. (2010). P-T evolution of Glenelg eclogites, NW Scotland: Did they experience ultrahigh-pressure metamorphism? Lithos, 114, 473-489.

Scambelluri, M., Pettke, T., van Roermund, H. (2008). Majoritic garnets monitor deep subduction fluid flow and mantle dynamics. Geology, 36, 59–62.

Schmadicke, E., and Muller, W. F. (2000). Unusual exsolution phenomena in omphacite and partial replacement of phengite by phlogopite + kyanite in an eclogite from the Erzgebirge. Contributions to Mineralogy and Petrology, 139, 629-642.

Schreyer, W., Massone, H. J., and Chopin, C. (1987). Continental crust subducted to depths near 100 km: implications for magma and fluid genesis in collision zones. In B. Mysen (Ed.), Magmatic Processes: Physiochemical Principles, p. 155-163. University Park: Geochemical Society.

Skogby, H. (1994). OH incorporation in synthetic clinopyroxene. American Mineralogist, 79, 240-249.

Skogby, H., and Rossman, G. (1989). OH- in pyroxene: An experimental study of incorporation mechanisms and stability. American Mineralogist, 74, 1059-1069.

Skogby, H., Bell, D. R., and Rossman, G. R. (1990). Hydroxide in pyroxene: Variations in the natural environment. American Mineralogist, 75, 764-774.

Smith, D. (1984). Coesite in clinopyroxene in the Calendonides and its implications for geodynamics. Nature, 310, 641-644.

Smith, D. C. (2006). The SHAND quaternary system for evaluating the supersilicic or subsilicic crystal-chemistry of eclogite minerals, and potential new UHPM pyroxene and garnet end-members. Mineralogy and Petrology, 88, 87-122.Smyth, J. R. (1980). Cation vacancies and the crystal chemistry of breakdown reactions in kimberlitic omphacites. American Mineralogist, 65, 1185-1191.

Smyth, J., Bell, D. R., and Rossman, G. R. (1991). Incorporation of hydroxyl in upper-mantle clinopyroxenes. Nature, 351, 732-735.

Sobolev, N., and Shatsky, V. S. (1990). Diamond inclusions in garnets from metamorphic rocks: a new environment for diamond formation. Nature, 343, 742-746.

Song, S., Yang, J. S., Xu, Z. Q., Liou, J. G., and Shi, R. D. (2003). Metamorphic evolution of hte coesite-bearing ultrahigh-pressure terrane in the North Qaidam, Northern Tibet, NW China. Journal of Metamorphic Geology, 21, 631-644.

Song, S., Bi, H., Qi, S., Yang, L., Allen, M., Niu, Y., Su, L., and Lu, W. (2018). HP-UHP metamorphic belt in the East Kunlun Orogen: Final closure of the Proto-Tethys Ocean and formation of the Pan-North-China continent. Journal of Petrology, 59, 2043-2060.

Spengler, D., Brueckner, H.K., van Roermund, H.L.M., Drury, M.R., Mason, P. (2009). Long-lived, cold burial of Baltica towards 200 km depth. Earth and Planetary Science Letters, 281, 27–35.

Sterner, S., and Bodnar, R. J. (1989). Synthetic fluid inclusions-VII. Re-equilibration of fluid inclusions in quartz during laboratory-simulated metamorphic burial and uplift. Journal of Metamorphic Geology, 7, 243-260.

Tsai, C., and Liou, J. G. (2000). Eclogite-facies relics and inferred ultrahigh-pressure metamorphism in the North Dabie Complex, central-eastern China. American Mineralogist, 85, 1-8.

van Breemen, O., Aftalion, M., Bowes, D. R., Dudek, A., Misar, Z., Povondra, P., et al. (1982). Geochronological studies of the Bohemian Massif, Czechoslovakia, and their significance in the evolution of Central Europe. Transactions of the Royal Society of Edinburgh, Earth Sciences, 73, 89-108.

Van Roermund, H., Carswell, D. A., Drury, M. R., and Heiboer, T. C. (2002). Microdiamonds in a megacrystic garnet websterite pod from Bardane on the island of Fjortoft, western Norway: evidence for diamond formation in mantle rocks during deep continental subduction. Geology, 30, 959-962.

Varela, M., Kurat, G., Clocchiatti, R., and Schiano, P. (1998). The ubiquitous presence of silica-rich glass inclusions in mafic minerals: Examples from Earth, Mars, Moon, and the aubrite parent body. Meteoritics and Planetary Science, 33, 1041-1051.

Veblen, D. R., and Cowley, J. M. (1994). Direct imaging of point defects in HRTEM. In A. Marfunin (Ed.), Advanced Mineralogy. Heidelberg: Springer-Verlag.

Vityk, M. O., Bodnar, R. J., and Dudok, I. V. (1995). Natural and synthetic re-equilibration textures of fluid inclusions in quartz (Marmarosh Diamonds): Evidence for refilling under conditions of compressive loading. European Journal of Mineralogy, 7, 1071-1087.

Wain, A. (1997). New evidence for coesite in eclogite and gneisses: Defining an ultrahigh-pressure province in the Western Gneiss region of Norway. Geology, 25, 927-930.

Wen, S., and Nekvasil, H. (1994). Ideal associated solutions: Application to the system albite-quartz-H_2O. American Mineralogist, 79, 316-331.

Withers, R., Thompson, J. G., and Welberry, T. R. (1989). The Structure and Microstructure of α-Cristobalite and its Relationship to β-Cristobalite. Physics and Chemistry of Minerals, 16, 517-523.

Wood, B., and Henderson, C. B. (1978). Composition and unit-cell parameters of synthetic non-stoichiometric tschermakitic clinopyroxenes. American Mineralogist, 63, 66-72.

Xu, H.F., Lee, S., and Xu, H.W. (2017) Luogufengite: a new nano-mineral of Fe_2O_3 polymorph with giant coercive field. American Mineralogist, **102**, 711-719.

Xu, S., Okay, A. I., Ji, S. Y., Sengor, A. M., Wen, S., Liu, Y. C., et al. (1992). Diamond from the Dabie-Shan metamorphic rocks and its implication for tectonic setting. Science, 256, 80-82.

Ye, K., Cong, B., and Ye, D. (2000). The possible subduction of continental material to depths greater than 200km. Nature, 407, 734-736.

Zhang, L., Song, S. G., Liou, J. G., Ai, Y. L., and Li, X. P. (2005). Relict coesite exsolution in omphacite from Western Tianshan eclogites, China. American Mineralogist, 90, 181-186.

Zhang, Z., Li, J., Jiang, Q. (2000). Modelling for size-dependent and dimension-dependent melting of nanocrystals. Journal of Physics D: Applied Physics, 33, 2653-2656.

Zhao, S., Nee, P., Green, W. H., and Dobrzhinetskaya, F. L. (2011). Ca-Eskola component in clinopyroxene: Experimental studies at high pressures and temperatures. Earth and Planetary Science Letters, 307, 517-524.

Zhu, Y., and Ogasawara, Y. (2002). Phlogopite and coesite exsolution from super-silicic clinopyroxene. International Geology Review, 44, 831-836.

FIGURE CAPTIONS

Figure 1. Plane polarized light photomicrograph of Bohemian Massif eclogite (a) and clinopyroxene (b). The rock (a) is dominated by garnets (black) and clinopyroxenes (most other grains in the image). Arrows point to decompression garnet/CPX and CPX/CPX symplectites; the symplectites are generally thin and the CPX grains are quite fresh, with little alteration. The lack of alteration can be seen in the cores of the clinopyroxenes (b), which are filled with siliceous precipitates. In this orientation viewed at an angle to the *c*-axis, the precipitates appear primarily as rods and some dots (likely rods on end). Precipitates are concentrated in the grain core, with few precipitates in the rims near grain boundaries. A black circle denotes one of the CPX grain boundaries at the top left of (b), where there is a much lower concentration of precipitates. Note that no optical evidence of volume change (i.e., cracking due to less dense phase transformation) surrounds the precipitates.

Figure 2. (a) Bright-field TEM image of α-cristobalite nano-crystal. Dominant euhedral diopside planes and α-cristobalite (101)α twin plane are labeled; nano-scale amphibole at cristobalite/diopside interface indicated with white arrow at top left of precipitate. White arrow at bottom of image highlights an area of great strain contrast, and may be a void. (b) SAED pattern details epitaxial orientation of diopside (black arrows/numbers on white box) with α-cristobalite (white arrows/numbers). (c) EDS spectrum from just the α-cristobalite nano-crystal. Simulated diffraction patterns (DP) with indexing of (d) both phases observed in the SAED pattern, only α –cristobalite (e), and only diopside (f). Diffraction spots from α-cristobalite spots which appear in the SAED (001, 002, 003), labeled as X's in the simulated diffraction pattern, are typically at extinction but appear due to multiple diffraction. (g) HRTEM image of nano-scale amphibole at interface of diopside and α-cristobalite.

Figure 3. (a) HRTEM image showing cristobalite domains in a twin relationship. Twin plane (101) corresponds to (111) in β-cristobalite. White squares are locations of Fast Fourier Transform (FFT) patterns in (c), which detail the crystallography on either side of the (101) twin plane. (b) Schematic representation of the α-cristobalite lattice with twinned unit cells in black; black arrows in (a, b, c) denote the location of the twin plane.

Figure 4. (a) Bright field TEM image of non-crystalline siliceous precipitate exhibiting "negative" pyroxene morphology. Dominant pyroxene planes evident in crystalline silica precipitates are also evident here. (b) Diffraction pattern is from the glass precipitate in (a). Ring with weak intensity, and possible diffraction spots are attributed to crystallites of an unidentified mineral that was quickly destroyed by the electron beam; (c) EDS spectrum from precipitate in (a). All non-crystalline precipitates possess Al in addition to Si, just as in this spectrum. (d-f) More examples of Al-bearing non-crystalline silica precipitates with negative pyroxene morphology.

Figure 5. (a) Non-crystalline siliceous precipitate in negative pyroxene shape surrounded by diopside (dark area). (b) SAED pattern shows evidence of a faint ring (white arrows point to the ring) likely contributed by the small crystals indicated by black arrows in the non-crystalline precipitate. (c) EDS spectrum shows there is some Al in the precipitate. (d) Diopside SAED pattern. (e) HRTEM image and (g, h) FFT patterns of diopside and Na-Ca-amphibole across the interface, respectively, detailing crystallographic orientation and excellent lattice fit of the single/double chains. (f) EDS spectrum from amphibole exhibits Na and Al.

Figure 6. (a) Low magnification TEM image and (b) HRTEM image of multiple sheet silicate crystals in diopside. Note euhedral [001] pyroxene shape of former silica precipitate is degraded, with few recognizable pyroxene planes evident. (c) EDS spectrum taken from the area in (b) showing Mg, Fe, and Al peaks, in addition to a large silica peak. Carbon peak is from carbon coating on sample. (d) SAED pattern from diopside. (e) SAED pattern from diopside and multiple mica crystals (f) SAED pattern from talc-like nano-crystals showing (001) reflections.

Figure 7. (a-d) Schematic representation of the structural relationship between diopside and α-cristobalite based upon SAED pattern. (a-c) are same orientation. (a, b) illustrate that diopside and cristobalite lattices join at the interface with little to no bending or rotation of silica tetrahedra. (a) $(010)_{Di} \parallel (-101)_{\alpha}$,. (b) $(-1-10)_{Di} \parallel (100)_{\alpha}$ (c-d) close lattice fit at the interface in (a, b) is shown utilizing unit cells of both crystals, where $(100)_{Di}$ is approximately $\parallel (101)_{\alpha}$. (c) $5d_{101\ a} = 20.2$ Å ~ $\parallel 2(a \bullet \sin\beta)\ d_{100\ CPX} = 18.6$ Å. (d) this diagram is the orientation in (c) rotated 90 degrees to look at CPX [010], and illustrates the structural match between $5d_{-101\alpha} = 20.2$ Å ~

‖ $2(a \bullet \sin\beta)\ d_{100\ CPX} = 18.6$ Å. The slight mismatch may cause the observed strain at the interface between diopside and cristobalite (Fig. 2a).

Figure 8: A diagram illustrating the pressure difference between the precipitates (curve c) and the host minerals (curve b). Melt inclusions will be over-pressured (curve a) with respect the host mineral. Modified from Burnham and Davis (1974).

TABLE CAPTION

Table 1. Recalculated EMPA clinopyroxene analyses from Bohemian Massif CPX grain, calculated with an assumed (not measured) Fe content of 2 wt. % Fe_2O_3; FeO = Fe – 2 wt % Fe_2O_3. Measurements made with 1μm beam. Oxygen calculated, all calculations based on 6 O. Potential calculated vacancy component = ([]).

This is a preprint, the final version is subject to change, of the American Mineralogist (MSA)
Cite as Authors (Year) Title. American Mineralogist, in press.
DOI: https://doi.org/10.2138/am-2019-6773

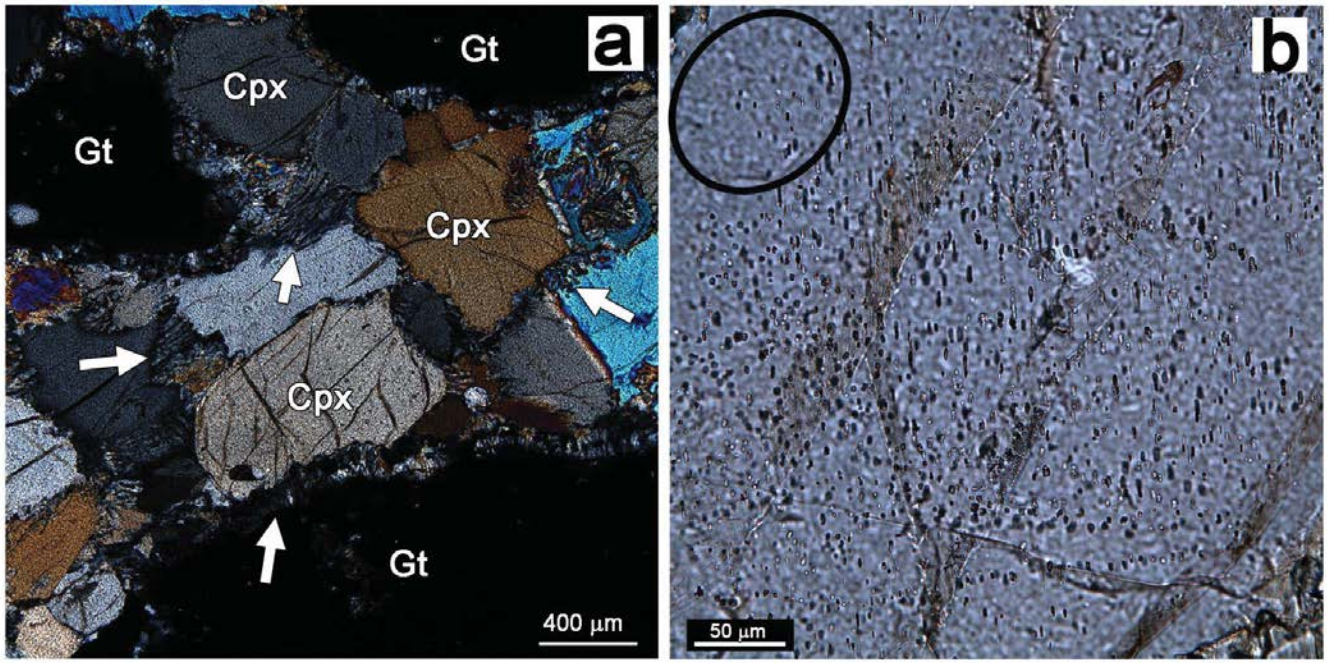

Fig. 1

This is a preprint, the final version is subject to change, of the American Mineralogist (MSA)
Cite as Authors (Year) Title. American Mineralogist, in press.
DOI: https://doi.org/10.2138/am-2019-6773

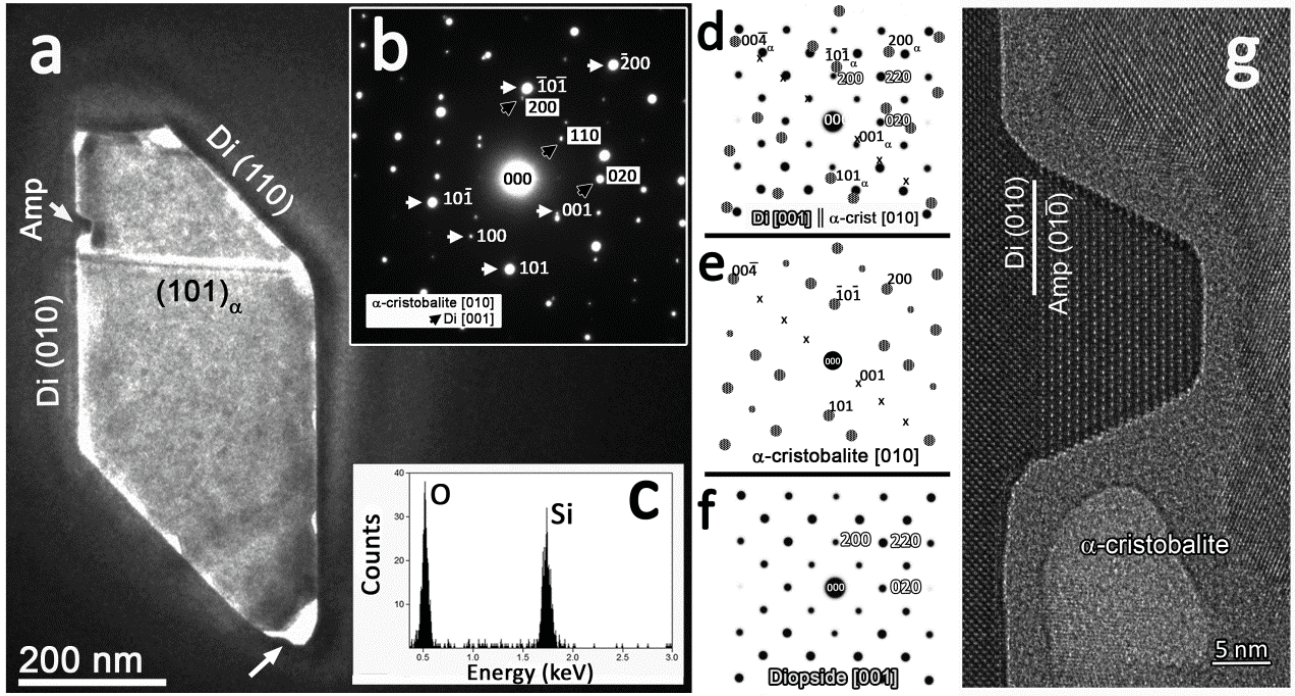

Fig. 2

This is a preprint, the final version is subject to change, of the American Mineralogist (MSA)
Cite as Authors (Year) Title. American Mineralogist, in press.
DOI: https://doi.org/10.2138/am-2019-6773

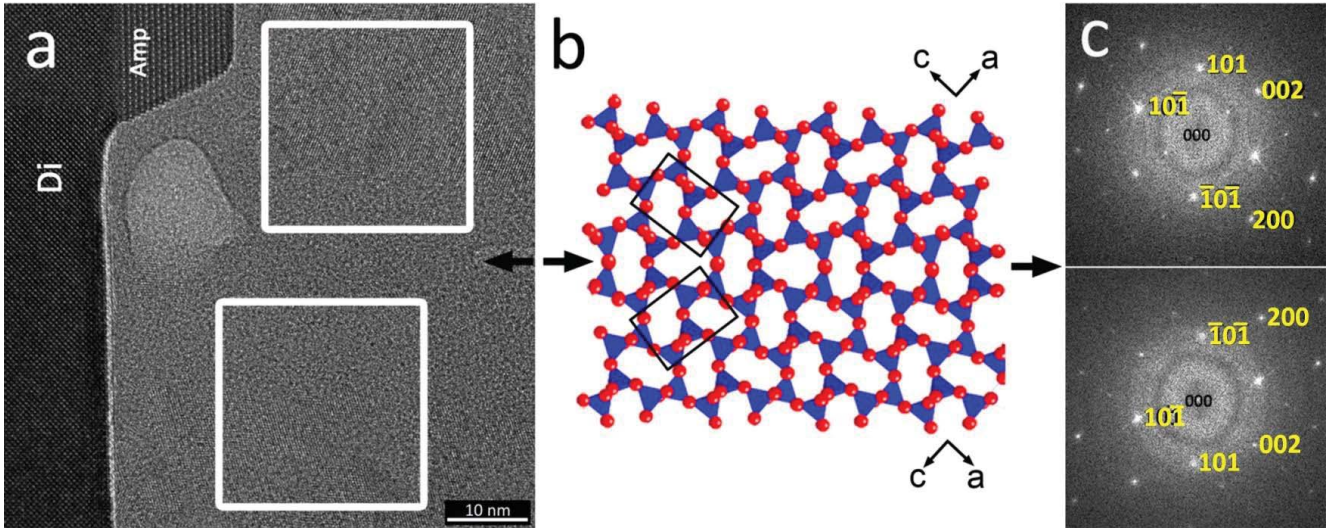

Fig. 3

This is a preprint, the final version is subject to change, of the American Mineralogist (MSA)
Cite as Authors (Year) Title. American Mineralogist, in press.
DOI: https://doi.org/10.2138/am-2019-6773

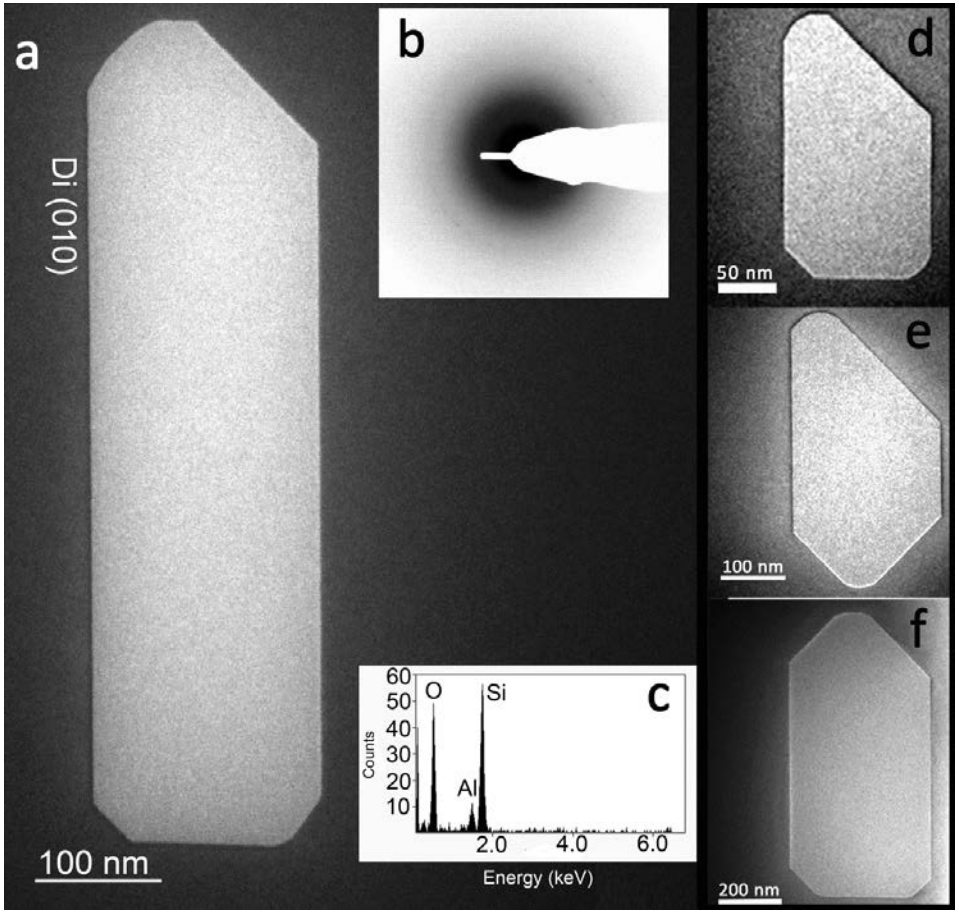

Fig. 4

This is a preprint, the final version is subject to change, of the American Mineralogist (MSA)
Cite as Authors (Year) Title. American Mineralogist, in press.
DOI: https://doi.org/10.2138/am-2019-6773

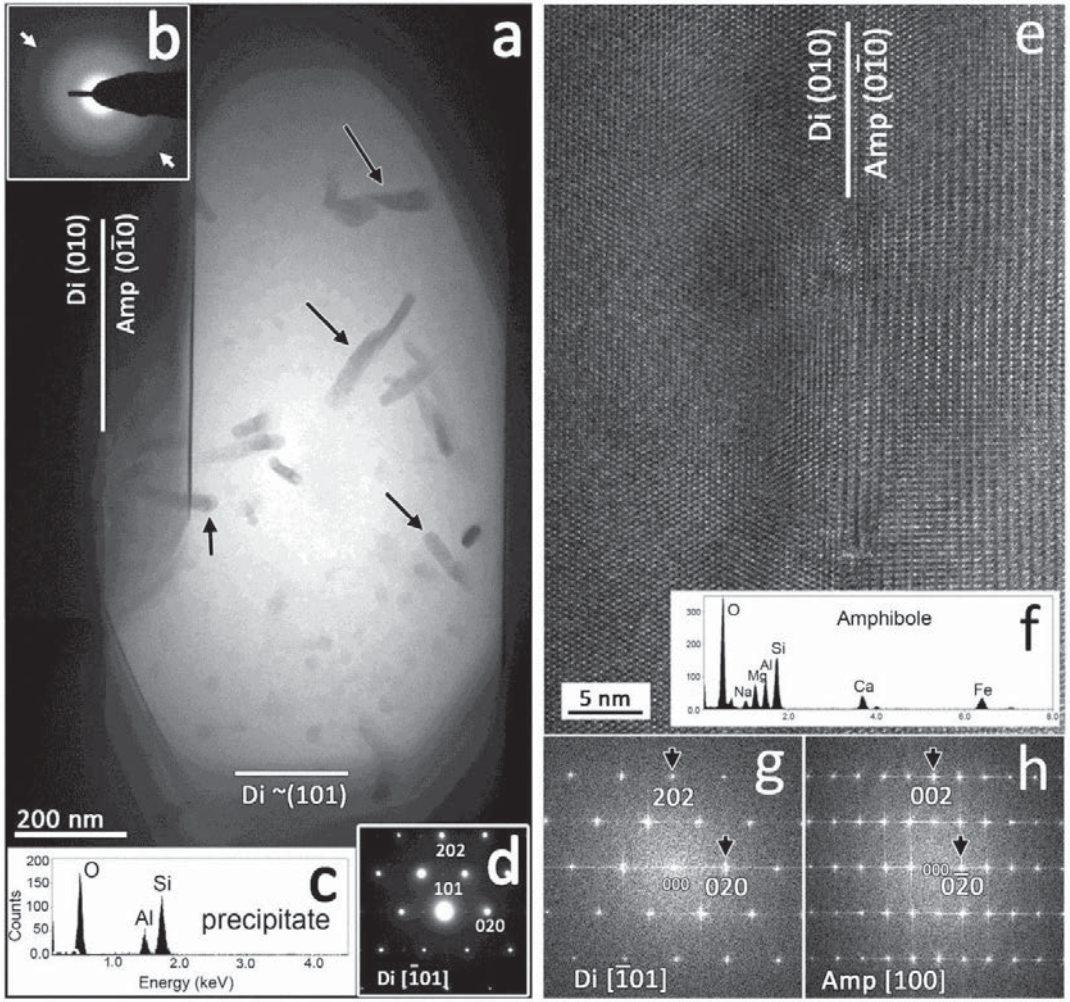

Fig. 5

This is a preprint, the final version is subject to change, of the American Mineralogist (MSA)
Cite as Authors (Year) Title. American Mineralogist, in press.
DOI: https://doi.org/10.2138/am-2019-6773

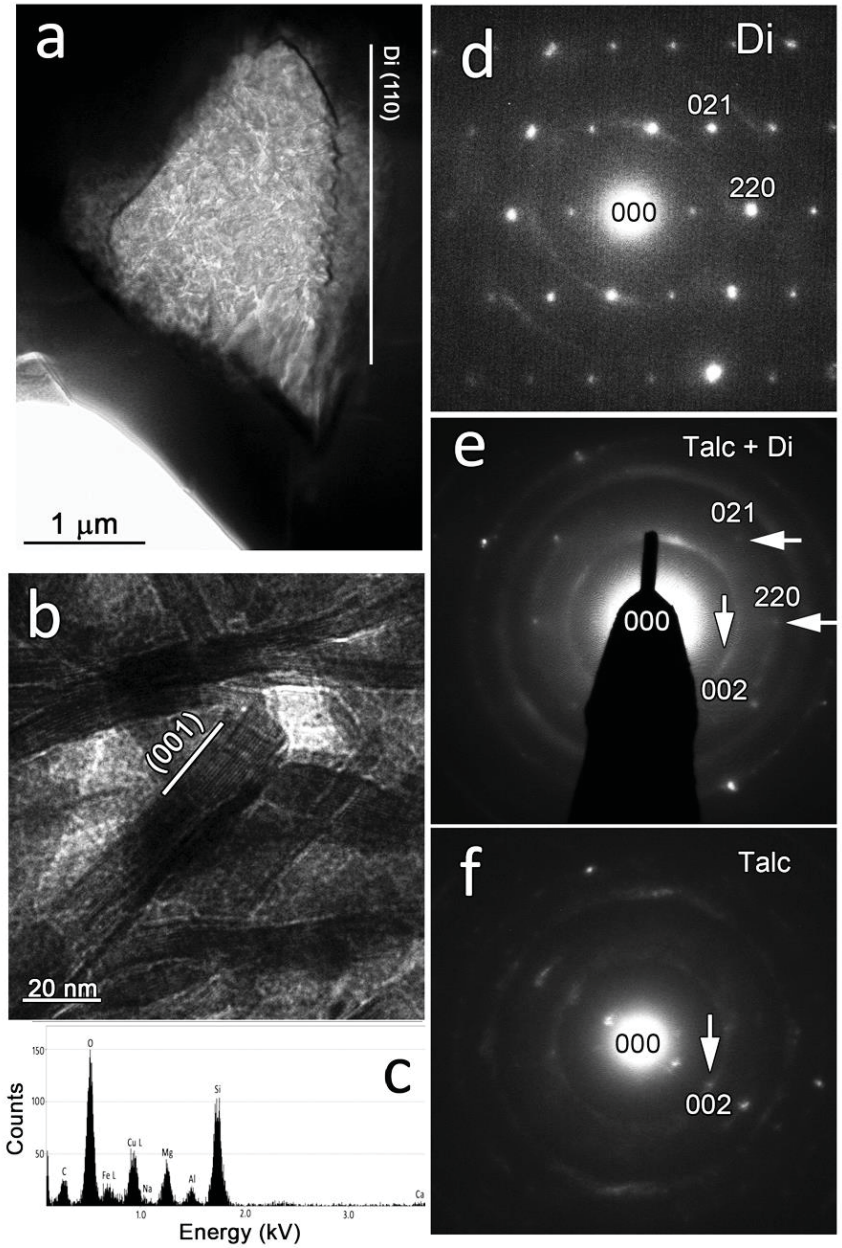

Fig. 6

This is a preprint, the final version is subject to change, of the American Mineralogist (MSA)
Cite as Authors (Year) Title. American Mineralogist, in press.
DOI: https://doi.org/10.2138/am-2019-6773

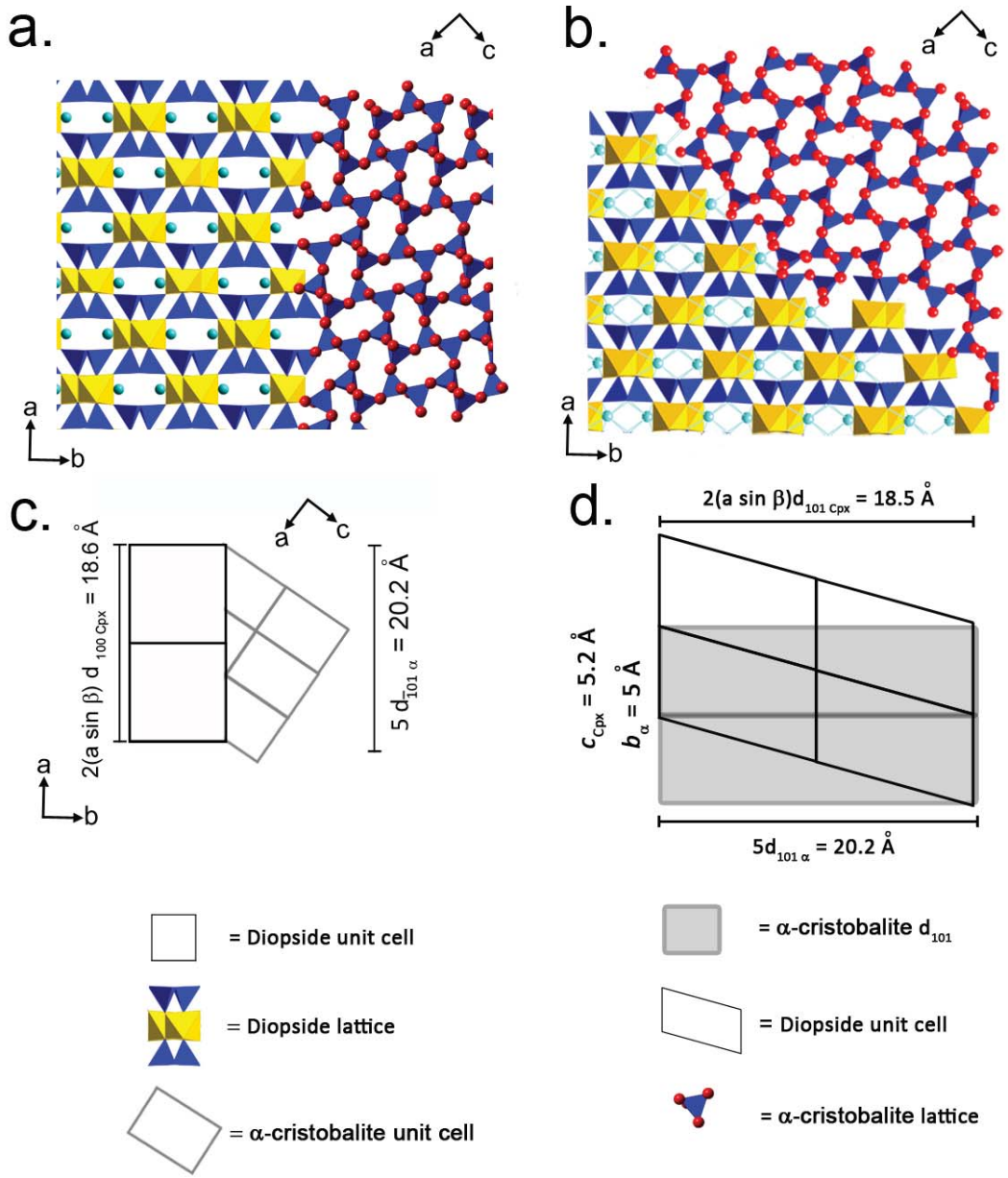

Fig. 7

This is a preprint, the final version is subject to change, of the American Mineralogist (MSA)
Cite as Authors (Year) Title. American Mineralogist, in press.
DOI: https://doi.org/10.2138/am-2019-6773

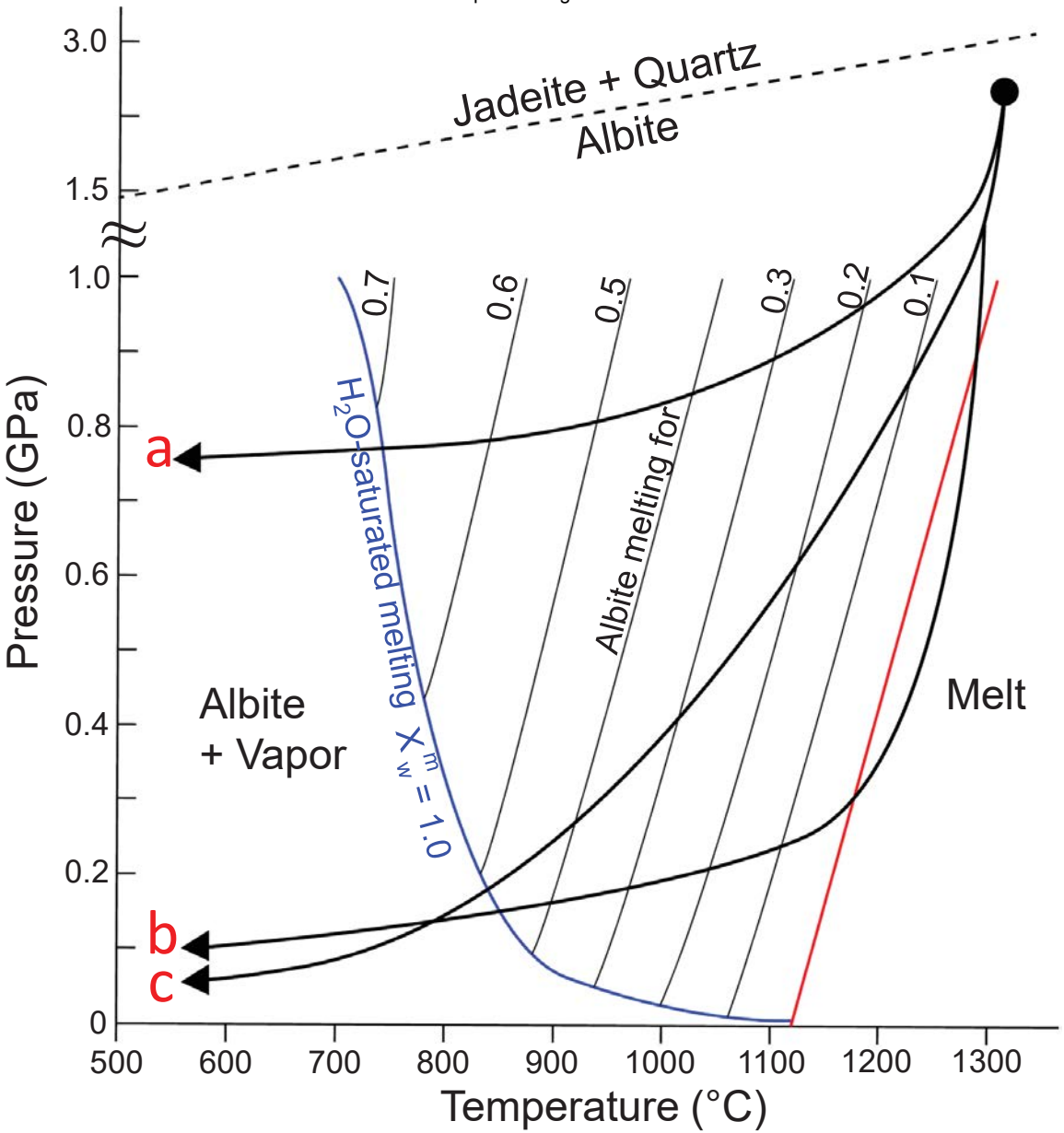

Fig. 8

Table 1. Recalculated EMPA clinopyroxene analyses from Bohemian Massif CPX grain, calculated with an assumed (not measured) Fe content of 2 wt. % Fe_2O_3; FeO = Fe – 2 wt % Fe_2O_3. Measurements made with 1μm beam. Oxygen calculated, all calculations based on 6 O. Potential calculated vacancy component = ([]).

Wt. % Oxide	Pt. 1	Pt. 2	Pt. 3	Pt. 4	Pt. 5	Pt. 6	Pt. 7	Pt.8	Pt. 9	Pt. 10	AVG	STDEV	SERR
SiO_2	52.88	53.11	53.50	53.32	53.48	53.73	53.24	53.12	52.93	53.11	53.24	0.26	0.08
TiO_2	0.20	0.30	0.32	0.34	0.25	0.27	0.35	0.36	0.38	0.26	0.30	0.06	0.02
Al_2O_3	8.39	7.67	7.38	7.63	7.62	7.63	8.05	7.99	8.26	8.34	7.90	0.36	0.12
Cr_2O_3	0.06	0.08	bd	bd	bd	0.09	bd	0.07	0.05	bd	0.07	0.04	0.01
FeO	3.18	3.06	3.24	3.01	3.38	3.11	3.10	3.23	3.45	3.11	3.19	0.14	0.04
Fe_2O_3*	2.00	2.00	2.00	2.00	2.00	2.00	2.00	2.00	2.00	2.00	n/a	n/a	n/a
MnO	0.07	0.01	0.01	bd	0.02	0.05	0.09	0.11	0.09	0.06	0.06	0.04	0.01
MgO	11.30	11.66	11.63	11.71	11.87	11.63	11.75	11.40	11.17	11.19	11.53	0.24	0.08
CaO	17.21	17.61	17.54	17.67	17.65	17.37	17.57	17.48	17.24	17.41	17.47	0.16	0.05
Na_2O	4.03	3.83	3.79	3.76	3.82	3.85	3.89	3.83	3.88	3.98	3.87	0.09	0.03
K_2O	0.00	bd	0.00	bd	0.02	0.02	0.01	bd	0.02	0.00	0.01	0.01	0.01
Total	99.32	99.34	99.41	99.43	100.10	99.74	100.06	99.60	99.47	99.46			
Si	1.944	1.955	1.970	1.960	1.959	1.970	1.944	1.953	1.949	1.952			
Ti	0.006	0.008	0.009	0.009	0.007	0.007	0.010	0.010	0.011	0.007			
^{IV}Al	0.056	0.045	0.030	0.040	0.041	0.030	0.056	0.047	0.051	0.048			
^{VI}Al	0.308	0.288	0.290	0.291	0.288	0.300	0.290	0.299	0.307	0.313			
Cr	0.002	0.002	bd	bd	bd	0.003	bd	0.002	0.001	bd			
Fe^{2+}	0.076	0.082	0.100	0.093	0.080	0.095	0.072	0.099	0.106	0.091			
Fe^{3+}	0.022	0.012	0.000	0.000	0.012	0.000	0.023	0.000	0.000	0.004			
Mn	0.002	0.000	0.000	bd	0.000	0.002	0.003	0.003	0.003	0.002			
Mg	0.619	0.640	0.638	0.642	0.648	0.636	0.640	0.625	0.613	0.613			
Ca	0.678	0.694	0.692	0.696	0.693	0.682	0.687	0.689	0.680	0.686			
Na	0.287	0.273	0.271	0.268	0.271	0.274	0.275	0.273	0.277	0.284			
K	0.000	0.000	0.000	0.000	0.000	0.000	0.000	0.000	0.001	0.000			
[] = CaEs	0.000	0.002	0.000	0.001	0.001	0.001	0.000	0.000	0.001	0.000			
Cations per 6 O	4.000	4.000	4.000	4.000	4.000	4.000	4.000	4.000	4.000	4.000			

Notes for Table 1:
bd = below detection
[]=vacancy component

* 2 wt. % Fe_2O_3 chosen for calculations, not measured

Cations per 6 O
Oxygen calculated

Statistics:
n=19
AVG= average
STDV= standard deviation
SERR= standard error